

To TDE or not to TDE: The luminous transient ASASSN-18jd with TDE-like and AGN-like qualities

J. M. M. Neustadt,^{1*} T. W.-S. Holoien,² C. S. Kochanek,^{1,3} K. Auchettl,^{4,5}
 J. S. Brown,⁵ B. J. Shappee,⁶ R. W. Pogge,¹ Subo Dong,⁷ K. Z. Stanek,¹
 M. A. Tucker,⁶ S. Bose,^{1,3} Ping Chen,⁷ C. Ricci,^{8,7,9} P. J. Vallely,¹ J. L. Prieto,^{8,10}
 T. A. Thompson,^{1,3} D. A. Coulter,⁵ M. R. Drout,¹¹ R. J. Foley,⁵ C. D. Kilpatrick,⁵
 A. L. Piro,² C. Rojas-Bravo,⁵ D. A. H. Buckley,¹² M. Gromadzki,¹³ G. Dimitriadis,⁵
 M. R. Siebert,⁵ A. Do,⁶ M. E. Huber,⁶ A. V. Payne⁶

¹Department of Astronomy, The Ohio State University, 140 West 18th Avenue, Columbus, OH 43210, USA

²The Observatories of the Carnegie Institution for Science, 813 Santa Barbara Street, Pasadena, CA 91101, USA

³Center for Cosmology and AstroParticle Physics (CCAPP), The Ohio State University, 191 W. Woodruff Avenue, Columbus, OH 43210, USA

⁴DARK, Niels Bohr Institute, University of Copenhagen, Lyngbyvej 2, 2100 Copenhagen, Denmark

⁵Department of Astronomy and Astrophysics, University of California, Santa Cruz, CA 95064, USA

⁶Institute for Astronomy, University of Hawai'i, 2680 Woodlawn Drive, Honolulu, HI 96822, USA

⁷Kavli Institute for Astronomy and Astrophysics, Peking University, Yi He Huan Road 5, Hai Dian District, Beijing 100871, China

⁸Núcleo de Astronomía de la Facultad de Ingeniería y Ciencias, Universidad Diego Portales, Av. Ejército 441 Santiago, Chile

⁹George Mason University, Department of Physics & Astronomy, MS 3F3, 4400 University Drive, Fairfax, VA 22030, USA

¹⁰Millennium Institute of Astrophysics, Santiago, Chile

¹¹Department of Astronomy and Astrophysics, University of Toronto, 50 St. George St., Toronto, ON M5S 3H4, Canada

¹²South African Astronomical Observatory, PO Box 9, Observatory 7935, Cape Town, South Africa

¹³Astronomical Observatory, University of Warsaw, Al. Ujazdowskie 4, 00-478 Warszawa, Poland

Accepted XXX. Received YYY; in original form ZZZ

ABSTRACT

We present the discovery of ASASSN-18jd (AT 2018bcb), a luminous optical/UV/X-ray transient located in the nucleus of the galaxy 2MASX J22434289–1659083 at $z = 0.1192$. Over the year after discovery, *Swift* UVOT photometry shows the UV SED of the transient to be well modeled by a slowly shrinking blackbody with temperature $T \sim 2.5 \times 10^4$ K, a maximum observed luminosity of $L_{\max} = 4.5_{-0.3}^{+0.6} \times 10^{44}$ erg s⁻¹, and a radiated energy of $E = 9.6_{-0.6}^{+1.1} \times 10^{51}$ erg. X-ray data from *Swift* XRT and *XMM-Newton* show a transient, variable X-ray flux with blackbody and power-law components that fade by nearly an order of magnitude over the following year. Optical spectra show strong, roughly constant broad Balmer emission as well as transient features attributable to He II, N III–V, O III, and coronal Fe. While ASASSN-18jd shares similarities with Tidal Disruption Events (TDEs), it is also similar to the newly-discovered nuclear transients seen in quiescent galaxies and faint Active Galactic Nuclei (AGNs).

Key words: accretion, accretion discs – black hole physics – galaxies: nuclei.

1 INTRODUCTION

Active galactic nuclei (AGNs) are known to vary, both photometrically and spectroscopically. These variations are likely driven by the variable accretion of material onto the supermassive black hole (SMBH) at the center of the galaxy, but there may also be contributions from variable obscura-

tion. While these variations have been studied for decades (e.g., [Andrillat 1968](#); [Tohline & Osterbrock 1976](#); [Oknyanskij 1978](#)), recent studies have continued to show a diversity of events that are qualitatively different from the typical, modest amplitude, stochastic variability observed in all AGNs (e.g., [MacLeod et al. 2012](#)). In particular, there are changing-look AGNs (e.g., [Bianchi et al. 2005](#); [Shappee et al. 2014](#); [MacLeod et al. 2016](#); [Trakhtenbrot et al. 2019b](#)), where a strong blue continuum and broad emission lines appear in

* E-mail: neustadt.7@osu.edu (JMMN)

and/or disappear from the spectrum of a known AGN over a range of timescales, “rapid turn-on” events or changing-look LINERs (e.g., Gezari et al. 2017a; Yan et al. 2019; Frederick et al. 2019), where a previously quiescent low-ionization nuclear emission region (LINER) galaxy transitions to an AGN, as well as other SMBH-driven transients that are not easily classified (e.g., Kankare et al. 2017; Tadhunter et al. 2017; Gromadzki et al. 2019; Trakhtenbrot et al. 2019a).

There are also rapid, luminous flares occurring in galaxies with previously quiescent galactic nuclei or faint AGNs that are believed to be Tidal Disruption Events (TDEs). TDEs are the result of a star crossing the tidal radius of the SMBH and being disrupted by tidal forces from the SMBH (Rees 1988; Phinney 1989; Evans & Kochanek 1989). Some of the disrupted material is then accreted onto the SMBH, producing a bright optical/UV/X-ray transient that fades over time. The relative amounts of accreted and ejected material, as well as the properties of the transient, are a combination of various physical processes, such as geometry of the original orbit (e.g., Guillochon & Ramirez-Ruiz 2013; Dai et al. 2018), the properties of both the disrupted star and SMBH (e.g., Guillochon & Ramirez-Ruiz 2013; Kochanek 2016), and radiative feedback from the accretion (e.g., Gaskell & Rojas Lobos 2014; Strubbe & Murray 2015; Roth et al. 2016; Roth & Kasen 2018). Previous studies of TDEs (e.g., Holoien et al. 2014; Auchettl et al. 2017) generally found that the energy radiated during the events are of order 10^{51} erg with mass equivalents of less than $0.01 M_{\odot}$ assuming an accretion efficiency of $\eta = 0.1$, suggesting that most of the bound debris is ejected and not accreted, or that the accretion efficiency is lower than expected. However, when one considers the energy emitted over much longer timescales, then the total radiated energy approaches $\sim 0.1 M_{\odot}$ (van Velzen et al. 2019b).

Compared to other extragalactic transients, such as supernovae (SNe) and AGN variability, TDEs have unique properties (see, e.g., Hung et al. 2017; Auchettl et al. 2018; Holoien et al. 2019a). The UV/optical spectral energy distributions (SEDs) of TDEs are well modeled by blackbodies with temperatures of a few 10^4 K. This is initially true for SNe, but SNe rapidly cool to below 10^4 K within weeks, whereas TDEs do not (see Figure 10 from Holoien et al. 2019a). The UV/optical SEDs of AGNs are usually best fit with power laws, $f_{\lambda} \propto \lambda^{-\alpha}$, rather than a single-temperature blackbody. A single-epoch AGN spectrum usually has $1 < \alpha < 2$ (Koratkar & Blaes 1999; Vanden Berk et al. 2001), whereas an AGN difference spectrum (i.e. the difference between bright and faint epochs) often has $\alpha \gtrsim 2$ (see, e.g., Ruan et al. 2014; Hung et al. 2016), thus becoming “bluer when brighter” (Wilhite et al. 2005). This is in line with theoretical predictions from a thin accretion disc model with a $T \propto R^{3/4}$ temperature profile, producing an SED with $\alpha \simeq 2.3$ in the optical/near UV (Shakura & Sunyaev 1973).

The light curves of TDEs usually peak and decay monotonically, but several TDEs show deviations from a monotonic decay. Examples are PS18kh/AT 2018zr (Holoien et al. 2019a; van Velzen et al. 2019a), which rebrightened multiple times after its initial decay, ASASSN-18ul/AT 2018fyk (Wevers et al. 2019b), which showed an extended plateau in its light curve, and ASASSN-19bt (Holoien et al. 2019b), which showed a short flare ~ 30 d before reach-

ing peak brightness. Additionally, there is some evidence that TDEs may fade more slowly as the SMBH mass increases (Blagorodnova et al. 2017; Wevers et al. 2017; van Velzen et al. 2019b). By contrast, AGN variability consists of stochastic, tenths-of-a-magnitude variation over periods of tens to hundreds of days (MacLeod et al. 2012).

Another distinction between TDEs and AGNs is their X-ray emission. TDEs usually have smaller column densities (N_{H}) and intrinsically softer spectra (e.g., ASASSN-14li: Brown et al. 2017; Kara et al. 2018) than that of AGNs. While TDEs show little variation in their hardness ratios as they fade, AGNs tend to become softer as they brighten and become harder as they fade (e.g., Auchettl et al. 2018).

The optical spectra of TDEs are usually dominated by very broad (FWHM $\gtrsim 10^4$ km s $^{-1}$) H and/or He II lines (e.g., Arcavi et al. 2014). Usually, the relative strengths of H to He II emission in an individual TDE are relatively constant, although there are counter examples: ASASSN-15oi had weak, transient H features (Holoien et al. 2018), while AT 2017eqx transitioned from being H-dominated to being He II-dominated (Nicholl et al. 2019). Many TDEs also show optical emission lines attributable to N III and O III (Blagorodnova et al. 2019; Leloudas et al. 2019). By contrast, optical spectra of Type 1 AGNs are dominated by broad H emission (FWHM ~ 2000 km s $^{-1}$) and narrow, collisionally excited lines like [O III] and [N II]. For Type 2 AGNs, the H emission lines are also narrow. The broad and narrow lines are thought to originate from different locations in the AGN, with the Broad Line Region (BLR) being closer to the SMBH than the Narrow Line Region (NLR) (Peterson 1993). AGNs will sometimes show weak He I emission and even weaker He II emission (Vanden Berk et al. 2001). While TDE emission lines generally become narrower as the continuum fades (e.g., Holoien et al. 2016a), the broad Balmer lines of AGNs show the opposite behavior, as predicted by photoionization models (Peterson et al. 2004; Denney et al. 2009).

Here we discuss ASASSN-18jd, a transient source first detected by the All-Sky Automated Survey for Supernovae (ASAS-SN, Shappee et al. 2014; Kochanek 2016) on 2018-04-09 (MJD 58217.4) at $(\alpha, \delta) = (22:43:42.866, -16:59:08.410)$. The event was coincident with the center of the galaxy 2MASX J22434289-1659083. We first reported the discovery of the transient to the Transient Name Server (TNS) on 2018-04-27 (MJD 58235.1) (Bersier & Stanek 2018), where it was designated AT 2018bcb. ASASSN-18jd was discovered after a seasonal gap due to Sun-constraints, and the last observation before the seasonal gap was on 2017-12-14 (MJD 58101.0), -116.4 d before detection. ASASSN-18jd was fading when discovered, so the peak brightness probably occurred during the gap. Throughout this paper, we use the date of first detection in the ASAS-SN data, MJD 58217.4, as a reference date for tracking the evolution of the transient. Using the H α emission features in our spectra (see Section 5), we find a redshift $z = 0.1192$ for ASASSN-18jd. This corresponds to a luminosity distance $D_L = 559.6$ Mpc for a flat universe with $h = 0.696$, $\Omega_M = 0.286$, and $\Omega_{\Lambda} = 0.714$ (Wright 2006). The Galactic extinction along this line-of-sight is $A_V = 0.098$ mag (Schlafly & Finkbeiner 2011). When we correct for extinction, we use a Cardelli et al. (1989) extinction curve with $R_V = 3.1$ throughout.

In Section 2, we describe the archival pre-outburst pho-

tometry of the host galaxy as well as the new photometry and spectroscopy for ASASSN-18jd. In Sections 3, 4, 5, and 6, we use this data to characterize the UV/optical SED, the X-ray properties, the optical spectra, and the UV spectra of ASASSN-18jd, respectively. We compare these properties to well-studied TDEs and to the typical properties of AGNs. In Section 7, we place ASASSN-18jd within the context of TDEs, conventional AGN variability, and the newly-discovered SMBH-driven transients.

2 OBSERVATIONS

In this section, we summarize the archival data available for the host galaxy and our new photometry and spectroscopy of ASASSN-18jd.

2.1 Host photometry

The available UV, optical, and IR photometry of the host galaxy 2MASX J22434289–1659083 is summarized in Table 1. The data come from the Galaxy Evolution Explorer (GALEX, Martin et al. 2005; Bianchi et al. 2011), Data Release 1 of Pan-STARRS (Pan-STARRS1, Chambers et al. 2016; Flewelling et al. 2016), the Two Micron All-Sky Survey (2MASS, Skrutskie et al. 2006) Extended Survey Catalog, and the Wide Infrared Survey Explorer (WISE, Wright et al. 2010). Due to the compactness of the galaxy, we used a region of $5''$ to derive the SED of the host, as this captures most of the emission of the galaxy in the relevant wavelengths. There were no archival observations available from the *Hubble Space Telescope* (*HST*), the *Chandra X-ray Observatory*, the *X-Ray Multi-Mirror Mission* (*XMM-Newton*), or the Dark Energy Survey (DES) Data Release 1. Due to its location in the southern sky, the host was not observed as part of the Sloan Digital Sky Survey (SDSS) or the VLA FIRST Survey. There are no previous outbursts or signs of V -band variability from the host galaxy between December 2005 and July 2010 in the 11 epochs of data from the Catalina Real-time Transient Survey (CRTS, Drake et al. 2009). The host has a WISE color of $(W1 - W2) = 0.28 \pm 0.04$ mag (Vega) which is bluer than most luminous AGNs with $(W1 - W2) \geq 0.8$ mag (Stern et al. 2012; Assef et al. 2013).

There is no source coincident with the host galaxy in the *ROSAT* All-Sky Survey (Voges et al. 1999; Boller et al. 2016). Assuming a power law of $\Gamma = 1.75$ and using the line-of-sight Galactic HI column density of $N_{\text{H}} = 2.71 \times 10^{20} \text{ cm}^{-2}$ (Kalberla et al. 2005), this yields a 3σ -upper limit on the X-ray flux in the 0.3–10.0 keV band of $F_{0.3-10} \lesssim 2 \times 10^{-12} \text{ erg s}^{-1} \text{ cm}^{-2}$, corresponding to a luminosity of $L_{0.3-10} \lesssim 7.5 \times 10^{43} \text{ erg s}^{-1}$ and $L_X/L_{\text{Edd}} < 0.015$ given our estimate of the SMBH mass (computed below). This limit does not exclude weak AGN activity, as surveys have found Type 1 and 2 AGNs at and below this X-ray luminosity (Tozzi et al. 2006; Marchesi et al. 2016; Liu et al. 2016; Ricci et al. 2017). There is also no source coincident with the host galaxy in the 1.4 GHz NRAO VLA Sky Survey (NVSS, Condon et al. 1998). This limits the flux density at 1.4 GHz to be $S(1.4 \text{ GHz}) \leq 2.5 \text{ mJy}$, corresponding to $L_\nu(1.4 \text{ GHz}) \leq 9.4 \times 10^{29} \text{ erg s}^{-1} \text{ Hz}^{-1}$. All of these factors

Table 1. Observed (left) and FAST-derived (right) $5''$ aperture AB magnitudes of host galaxy 2MASX J22434289–1659083. Errors are assumed to be 0.1 mag (0.2 mag for GALEX).

Filter	Observed	Synthetic
GALEX NUV	21.11	20.98
PS g	17.77	17.83
PS r	16.99	16.97
PS i	16.55	16.57
PS z	16.34	16.28
PS y	16.10	16.10
2MASX J	15.61	–
2MASX H	15.78	–
WISE W1	16.16	–
WISE W2	16.53	–
<i>Swift</i> UVW2	–	20.99
<i>Swift</i> UVM2	–	21.01
<i>Swift</i> UVW1	–	20.82
<i>Swift</i> U	–	19.77
<i>Swift</i> B	–	18.54
<i>Swift</i> V	–	17.33
SDSS u'	–	19.61
SDSS g'	–	17.98
SDSS r'	–	16.96
SDSS i'	–	16.54

imply that any pre-event AGN activity must be relatively weak, if present at all.

We used the archival GALEX, Pan-STARRS1, and WISE fluxes to model the host galaxy’s SED with the code Fitting and Assessment of Synthetic Templates (FAST; Kriek et al. 2009). In doing the fits, we assumed minimum errors of 0.1 mag to account for potential systematic errors, except for the GALEX data, where we used the reported errors of 0.2 mag. We included Galactic extinction, an exponentially declining star-formation history, a Salpeter initial mass function, and the Bruzual & Charlot (2003) stellar population models. Our best fit had a stellar mass of $M_* = 1.7^{+0.1}_{-0.9} \times 10^{11} M_\odot$, age = $8.9^{+0.6}_{-5.9}$ Gyr, and a star formation rate of $\text{SFR} = 0.6^{+0.1}_{-0.3} M_\odot \text{ yr}^{-1}$. We combined the SED fit generated by FAST and the appropriate filter profiles to produce our synthetic photometry. Table 1 compares these FAST-derived magnitudes to the data and provides estimates of the host flux in the *Swift* and SDSS bands.

We used the stacked Pan-STARRS1 g - and r -band images and the galaxy image decomposition program GALFIT (Peng et al. 2002) to estimate the bulge-to-total light ratio, B/T . We found $(B/T)_g \approx 0.18 \pm 0.05$ and $(B/T)_r \approx 0.16 \pm 0.05$. Using these ratios, we assumed $(B/T)_V \approx 0.17 \pm 0.10$, corresponding to a bulge luminosity of $\log L_V/L_\odot = 9.6 \pm 0.3$ using the synthetic V -band luminosity from FAST. This was done after correcting for the $5''$ aperture of the synthetic FAST flux, but because the galaxy is relatively compact, this correction changed B/T by only ~ 0.01 , well within the uncertainties. Using the $M_{\text{BH}}-L_V$ relation from McConnell & Ma (2013), the SMBH mass is then $\log M_{\text{BH}}/M_\odot = 7.6 \pm 0.4$. The dispersion in the $M_{\text{BH}}-L_V$ relation is much larger than any reasonable uncertainties in B/T . While this mass is significantly larger than most SMBH masses associated with TDEs (Wevers et al. 2017, 2019a), it is still in the mass range where main sequence stars can be disrupted before crossing the event horizon (see, e.g., Kochanek 2016).

2.2 ASAS-SN photometry

We show the full ASAS-SN g - and V -band light curve before and during the transient in Figure 1, where the flux of the host galaxy has been subtracted. We also show the upper limit on the pre-transient g -band flux from November and December 2017 of $g > 20.09$ mag. The V -band photometry from November 2013 to December 2017 shows no obvious variability, similar to what we see in the CRTS data. Some epochs show faint “detections” of transient flux from the host, but these are very likely artefacts from image subtraction, as none of these “detections” are consistent across nearby epochs. The last pre-transient epochs of observation for g and V band were 2017-11-29 (MJD 58086.1) and 2017-12-14 (MJD 58101.0), respectively. We use the latter date, MJD 58101.0, 116.4 d before the date of first detection, as the beginning of the seasonal gap, which we later use to constrain the evolution of the transient in Section 3. Because ASAS-SN stopped using V band in late 2018, there is no V -band photometry after MJD 58447.2.

2.3 *Swift* photometry

We monitored ASASSN-18jd (Target ID: 10680; PI: T. Holoién) with the *Swift* UVOT telescope (Roming et al. 2005) in the V (5468 Å), B (4392 Å), U (3465 Å), $UVW1$ (2600 Å), $UVM2$ (2246 Å), and $UVW2$ (1928 Å) filters. Each epoch of UVOT data consists of 2 observations in each filter which we combined. We then extracted counts from a $5''.0$ radius around the source and use the background counts from a region with no sources and a radius $\sim 40''$. For these two steps we use the HEASoft software tasks UVOTIMSUM and UVOTSOURCE, respectively. The counts were then converted to AB magnitudes and fluxes using the most recent UVOT calibrations (Poole et al. 2008; Breeveld et al. 2010). Altogether, we obtained 50 epochs of *Swift* observations from MJD 58249.8 (+32 d) to MJD 58661.4 (+444 d). There is a gap in the *Swift* data from MJD 58489 (early January 2019) to MJD 58598 (mid April 2019) due to ASASSN-18jd becoming Sun-constrained.

Simultaneous with our *Swift* UVOT observations, we observed ASASSN-18jd in photon-counting (PC) mode with the *Swift* X-ray Telescope (XRT, Burrows et al. 2005). All observations were reduced following the standard *Swift* XRT data reduction guide¹, and reprocessed using the *Swift* XRT-PIPELINE version 0.13.2 script. Standard filters and screening were applied, along with the most up-to-date calibration files. We used a source region centered on the position of ASASSN-18jd with a radius of $30''$ and a source free background region centered at $(\alpha, \delta) = (22:43:50.482, -16:54:32.90)$ with a radius of $200''$. We corrected our count rate for the encircled energy fraction (~ 90 per cent at 1.5 keV for a $30''$ radius, Hill et al. 2004). We were also able to combine our *Swift* XRT observations into two time bins covering the first and last ~ 200 d of our monitoring program to extract both a source and background spectrum. We merged our observations using XSELECT version 12.9.1c, and then use the task XRTPRODUCTS and the same extraction regions. Ancillary response files for each spectra are generated

¹ http://swift.gsfc.nasa.gov/analysis/xrt_swguide_v1_2.pdf

using the task XRTMKARF, along with the standard response matrix files from CALDB. A summary of these observations is included in Table 4.

2.4 *XMM-Newton* observations

Because ASASSN-18jd was X-ray bright, we requested two deep *XMM-Newton Observatory* target of opportunity observations of the source. The first observation was taken on 2018-05-28 (MJD 58266.8; ObsID: 0830191201, PI: Scharrel/Ricci), approximately +49 d after the initial discovery, while our second observation was taken two weeks later on 2018-06-11 (MJD 58280.6; ObsID: 0830191301, PI: Scharrel/Ricci), approximately +63 d after the initial discovery. Both the MOS and PN detectors were used for this analysis and both observations were obtained in full frame mode using a thin filter. All data reduction and analysis was done using the *XMM-Newton* science system (SAS) version 17.0.0 (Gabriel et al. 2004) with the most up to date calibration files.

To check for periods of high background activity that may affect the quality of the data, we generated count rate histograms of the events that have energies between 10–12 keV for each observation. We found that both observations are only slightly affected by background flares, giving effective exposure times of 32 ks, 32 ks, and 28 ks for the MOS1, MOS2 and PN detectors, respectively for the first observation and 24 ks, 24 ks, and 21 ks, respectively, for the second observation. A summary of these observations is included in Table 4.

For our analysis we used the standard screening of events as specified in the *XMM-Newton* analysis guide for the MOS and PN detectors². We also corrected all event files for possible vignetting using the task EVIGWEIGHT³. We extracted spectra from both the MOS and PN detectors of ASASSN-18jd using the SAS task EVSELECT and the cleaned event files from all detectors. We used the same source region that was used to analyse the *Swift* observations with a radius of $30''$, while we used a source free background region centered at $(\alpha, \delta) = (20:43:25.495, -16:58:58.60)$ with a radius of $70''$. All spectra were binned with a minimum of 20 counts per energy bin using the FTOOLS command GRPPHA, and we used the X-ray spectral fitting package (XSPEC) version 12.10.0 (Arnaud 1996) and chi-squared statistics to analyse the spectra. Count rates were also extracted from the PN observations using the same regions and corrected for encircled energy fraction⁴. These data and their analysis are further discussed in Section 4.

2.5 Ground-based optical photometry

We obtained photometric observations from multiple ground-based observatories. *BVgri* observations were obtained using the Las Cumbres Observatory (Brown et al.

² https://xmm-tools.cosmos.esa.int/external/xmm_user_support/documentation/sas_usg/USG/

³ <https://xmm-tools.cosmos.esa.int/external/sas/current/doc/evigweight>

⁴ <https://heasarc.nasa.gov/docs/xmm/uhb/onaxisxraypsf.html>

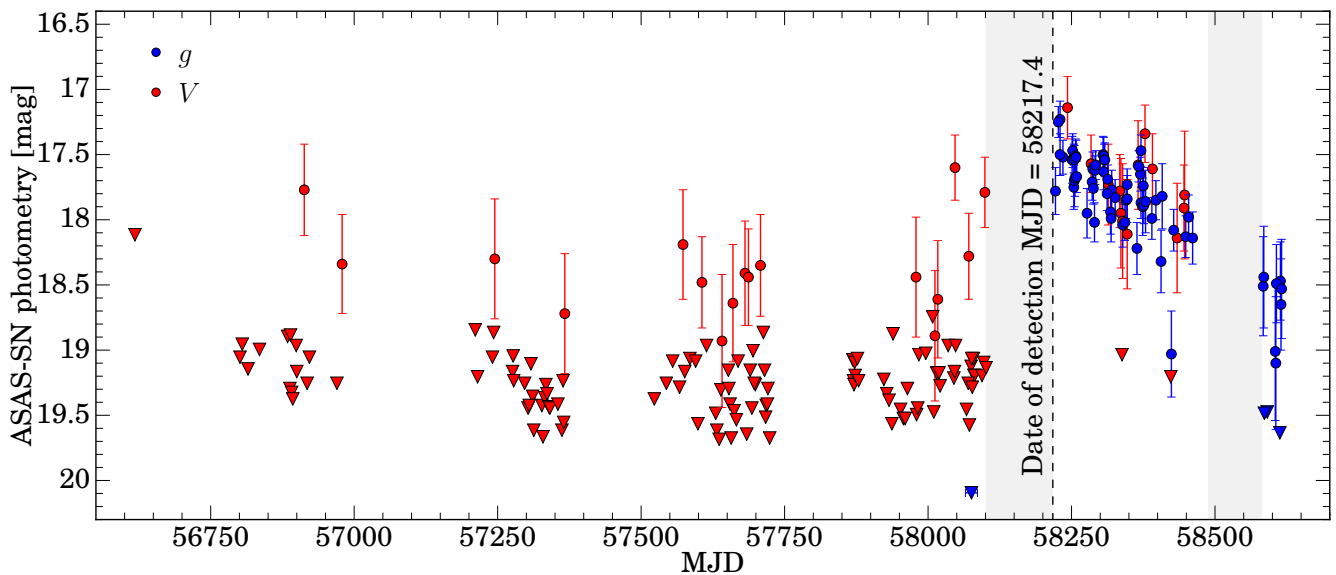


Figure 1. ASAS-SN photometry of ASASSN-18jd in g - (blue) and V - (red) band magnitudes. Detections are presented as circles, and 3σ upper limits are triangles. The transient photometry excludes the flux of the host, and the pre-transient “detections” are almost certainly artefacts of image subtraction. The 3σ upper limit on the average pre-transient g -band variability for Nov and Dec 2017 (MJD ~ 58060 – 58100) is also shown. The seasonal gaps, where no data were collected in epochs relevant to the transient, are shaded.

2013) 1-m telescopes located at the Cerro Tololo Inter-American Observatory (CTIO) in Chile, McDonald Observatory in Texas, Siding Spring Observatory in Australia, and the South African Astronomical Observatory (SAAO). $uBVgri$ observations were obtained with the Swope 1-m telescope at Las Campanas Observatory in Chile. BV observations were obtained with A Novel Dual Imaging Camera (ANDICAM; DePoy et al. 2003) on the SMARTS 1.3-m telescope at CTIO.

After applying flat-field corrections, we solved for the astrometry of the field using the `astrometry.net` package (Barron et al. 2008; Lang et al. 2010). We then measured $5''$ aperture magnitudes of the transient and host galaxy using the IRAF `apphot` package. We obtained archival $grizy$ magnitudes of several stars in the field with well-defined magnitudes from Pan-STARRS1 (Chambers et al. 2016; Flewelling et al. 2016). We calculated SDSS $ugriz$ magnitudes for these stars using the conversions found in Finkbeiner et al. (2016) and used these to calibrate the transient magnitudes measured in our follow-up $ugriz$ data. BV follow-up data were calibrated using stars in SDSS and the $ugriz$ to BV transformations from Lupton 2005⁵. A full summary of the photometry, including *Swift* and ASAS-SN photometry, is presented in Table 3.

In order to obtain a more accurate position of the transient than that provided by ASAS-SN, which has $7''$ pixels, we solved the astrometry for two Swope g -band images when the transient was bright and dim. After subtracting these two images to produce an image containing only the transient, we then calculated the position of the transient using the IRAF `imcentroid` package. This yields a posi-

tion of $(\alpha, \delta) = (22:43:42.866, -16:59:08.410)$ for ASASSN-18jd. We also found the center of the host galaxy using the archival g -band Pan-STARRS1 image to be $(\alpha, \delta) = (22:43:42.862, -16:59:08.309)$, yielding an angular offset of $0''.12 \pm 0''.01$, where the uncertainty only incorporates potential uncertainty with the centroid positions. We used the same procedure to measure the positions of several stars in both the Swope g -band image and the Pan-STARRS g -band image, and find an average random offset of $0''.20$ between the two images. Our measured offset of the transient is thus consistent with the center of the host, given the random offsets between the images.

2.6 Optical spectroscopy

We obtained multi-epoch optical spectra of ASASSN-18jd spanning 240 d from 2018-05-13 (MJD 58251.4; +34 d) until 2019-06-28 (MJD 58662.4; +445 d) using the Robert Stobie Spectrograph (RSS, Burgh et al. 2003; Kobulnicky et al. 2003) on the South African Large Telescope (SALT, Buckley et al. 2006), the Multi-Object Double Spectrographs (MODS, Pogge et al. 2010) on the dual 8.4-m Large Binocular Telescope (LBT), the Wide Field Reimaging CCD Camera (WFCCD, Weymann et al. 2001) on the 2.5-m du Pont telescope at Las Campanas Observatory, the Kast Double Spectrograph on the 3-m Shane Telescope at Lick Observatory, and the Supernova Integral Field Spectrograph (SNIFS, Lantz et al. 2004) on the University of Hawaii 88-in telescope. A synopsis of the spectra is given in Table 5. The ePESSTO collaboration, using a spectrum taken ~ 7 d before our first spectrum, classified the event as an AGN (McBrien et al. 2018).

The majority of these spectra were reduced using standard IRAF/PyRAF procedures, including bias subtracting,

⁵ <http://www.sdss.org/dr5/algorithms/sdssUBVRITransform.html>

flat fielding, wavelength fitting using comparison arc lamps, and flux calibration using spectroscopic standard stars. The MODS spectra were reduced using the MODS spectroscopic pipeline⁶. Flux calibration with SALT is difficult because of the telescope design, which has a moving, field-dependent and under-filled entrance pupil. Observations of spectrophotometric flux standards can, at best, only provide relative flux calibration (see, e.g., Buckley et al. 2018), which mostly accounts for the telescope and instrument sensitivity changes as a function of wavelength.

To combat these issues, we calibrated our SALT spectra using the ground-based photometry. We re-measured our Swope and Las Cumbres Observatory data using smaller 1.75 apertures to approximate the slit widths of the spectra and thus account for host contamination. We then extracted synthetic photometry from our spectra and compared the differences as a function of the central wavelength of the filters. Fitting a line between these differences, we scaled the spectra so as to match the smaller aperture photometry. We repeated this process for the du Pont, Kast, MODS, and SNIFS spectra so that that our data reduction was consistent. We also corrected for Galactic extinction. In general, we focus on the emission and absorption features in the spectra rather than the continuum shape.

The SNIFS spectra were taken from Maunakea, HI at a relatively high airmass, and some of the spectra were obtained under poor weather conditions. As a result, the spectra have a very weak blue continuum, and only some of the spectra show faint emission features blueward of H β . Additionally, SNIFS’s dichroic is located at 4800–5300 Å (host rest-frame \sim 4300–4800 Å), making measurements in that range unreliable. For this reason, we only show the SNIFS spectra redward of rest-frame 4800 Å.

2.7 HST/STIS UV spectroscopy

We obtained 6 observations using *HST*’s Space Telescope Imaging Spectrograph (STIS; Woodgate et al. 1998) and the FUV/NUV MAMA detectors. We used the 52.0' \times 0.2' slit and the G140L (1150–1730 Å, FUV-MAMA) and G230L (1570–3180 Å, NUV-MAMA) gratings. The details of the exposures for each epoch are shown in Table 6. The source was clearly detected in the two-dimensional frames and spatially unresolved, so we used the standard *HST* pipeline for producing one-dimensional spectra. We performed inverse-variance-weighted combinations of the individual exposures, merged the FUV and NUV channels, and corrected for Galactic extinction.

3 SED ANALYSIS

We correct our photometry for Galactic extinction and subtract the synthetic host magnitudes from Table 1 to create UV-optical light curves and temporally-resolved SEDs of the event. The evolution of the extinction-corrected, host-subtracted photometry is shown in Figure 2. Our photometry shows that ASASSN-18jd is fading, albeit slowly. The

average decay rates in rest frame days in the *Swift* UVW1 and UVW2 filters were 3.3 mag d⁻¹.

While the transient is fading overall, there are multiple bumps in the light curve near +90 d, +150 d, and +260 d. These bumps are especially prominent in the UV, although there appear to be similar, weaker bumps in the *B*- and *g*-band light curves. When we remove the roughly linear decay seen in the light curve, the RMS variability in *Swift* UVW2, UVM2, UVW1, *U*, and *B* bands is 0.15, 0.14, 0.12, 0.12 and 0.13 mag, respectively, all of which are larger than the median errors of 0.5, 0.5, 0.5, 0.7, and 0.12 mag, respectively. This is unusual for TDEs, which generally show fairly smooth declines (Holoien et al. 2019b). For example, the light curve of ASASSN-19bt had RMS variability of only \sim 0.01 mag. However, these variations are not unusual for AGNs, which vary stochastically.

We fit blackbody models to the host-subtracted *Swift* fluxes using Markov chain Monte Carlo (MCMC) methods. A complete SED of ASASSN-18jd is shown in Figure 3. The median *Swift* photometry and blackbody fits for four ranges of epochs are shown. The FAST model of the host SED is added for comparison. We show the evolution of the bolometric luminosity, effective temperature, and effective radius in Figure 4. All 6 *Swift* filters were not available for some epochs, and the uncertainties on our fits are larger in the epochs with missing filters. Two epochs had only one or two filters and are not included in the blackbody fits.

The top-left panel of Figure 4 shows the evolution of the luminosity of ASASSN-18jd as compared to the TDEs ASASSN-14ae (Holoien et al. 2014; Brown et al. 2016), ASASSN-14li (Holoien et al. 2016a; Brown et al. 2017), ASASSN-15oi (Holoien et al. 2016b, 2018), iPTF16fnl (Brown et al. 2018), and PS18kh (Holoien et al. 2019a). As seen in the photometry, the overall luminosity of the transient decreases very slowly. We calculate a maximum luminosity of $L_{\max} = 4.5_{-0.3}^{+0.6} \times 10^{44}$ erg s⁻¹ = $1.2 \times 10^{11} L_{\odot}$. Our mass estimate for the SMBH yields an Eddington luminosity of $L_{\text{Edd}} = 4.9 \times 10^{45}$ erg s⁻¹, and thus the maximum luminosity corresponds to $L_{\max}/L_{\text{Edd}} = 0.092$. Because of the seasonal gap before discovery, we likely did not observe the event at peak brightness, and thus the peak luminosity was probably closer to L_{Edd} . The bumps seen in the photometry are also seen in the luminosity evolution.

We fit the evolution of the luminosity in rest frame days as a power law $L \propto (t - t_0)^{-\alpha}$. Because ASASSN-18jd was discovered after a seasonal gap and as it was fading, it is possible that the transient started up to -116.4 d before the discovery on MJD 58217.4. This affects the best fit for α . To show this, we compute power-law fits using two different t_0 , corresponding to the beginning ($t_1 = 58101.0$) and the end ($t_2 = 58217.4$) of the seasonal gap. These yield $\alpha_1 = 0.856 \pm 0.049$ ($\chi^2_{\nu} = 3.60$, dof = 46) and $\alpha_2 = 0.431 \pm 0.031$ ($\chi^2_{\nu} = 5.56$, dof = 46), respectively. Thus, if the decay follows a power law, it must have an index of $0.43 \lesssim \alpha \lesssim 0.86$, which is slower than the “canonical” TDE decay rate of $t^{-5/3}$ yet faster than the $t^{-5/12}$ disc-dominated model of Lodato & Rossi (2011). We also fit the evolution of the luminosity as an exponential, $L \propto e^{-t/\tau}$, where a changing t_0 does not affect the best-fitting parameters. The best fit for the exponential profile is $\tau = 311.9 \pm 14.5$ d ($\chi^2_{\nu} = 2.24$, dof = 46). At early times, this decay rate is much slower than $t^{-5/3}$. Formally,

⁶ <http://www.astronomy.ohio-state.edu/MODS/Software/modsIDL/>

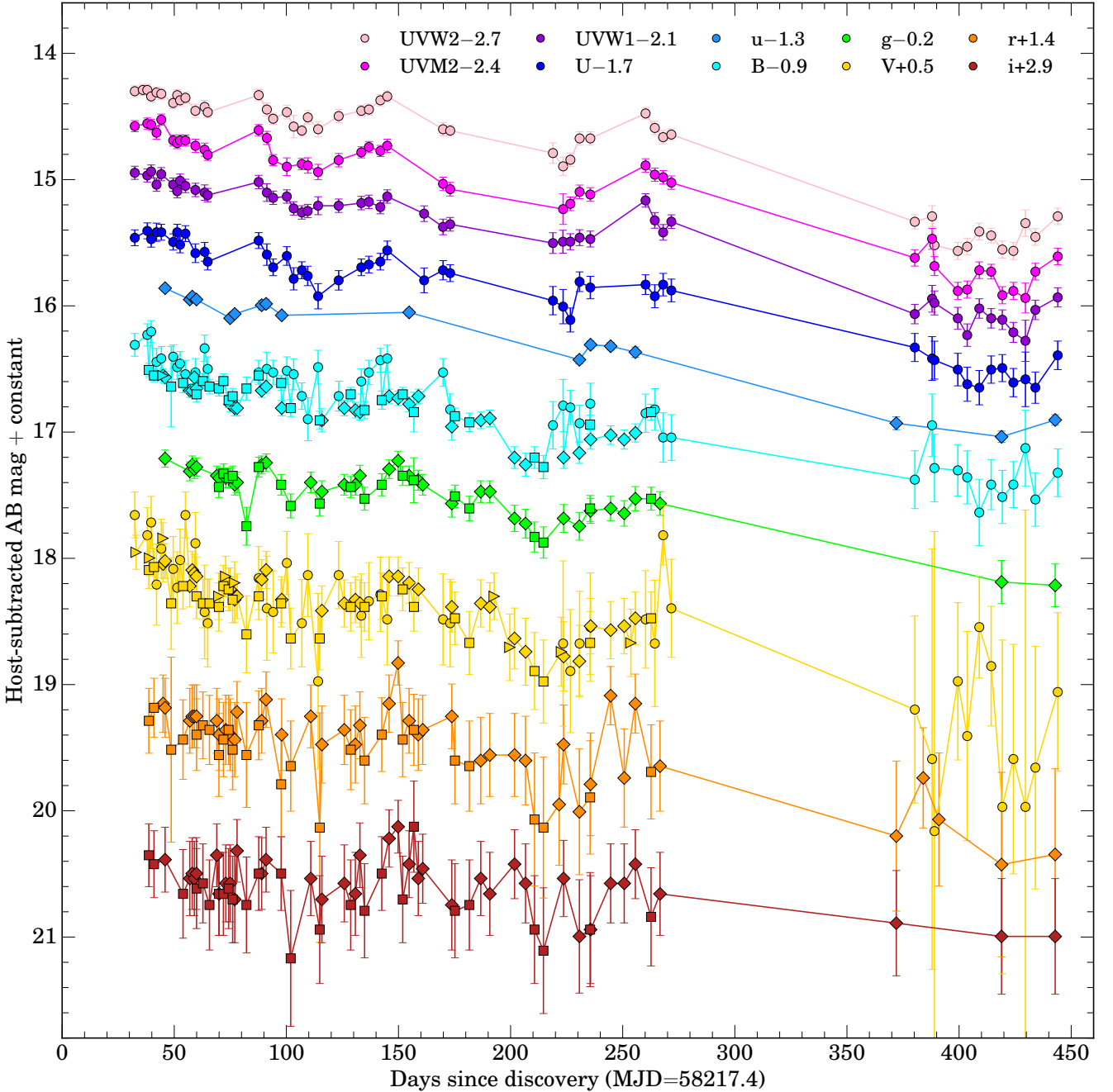


Figure 2. *Swift* UVOT and ground-based photometry of ASASSN-18jd that has been corrected for Galactic extinction and host-subtracted with the FAST-derived SED. The magnitudes are in the AB system. Circles correspond to data from *Swift*, diamonds from Swope, squares from Las Cumbres, and triangles from SMARTS. Days are in observed days, rather than rest-frame days.

with such high χ^2_ν , all of the fits are poor, driven by the multiple bumps in the light curve.

The top-right panel of Figure 4 shows the evolution of the effective temperature of ASASSN-18jd compared to the effective temperatures of the TDEs. The effective temperature of ASASSN-18jd has remained roughly constant at $T = (2.5 \pm 0.3) \times 10^4$ K, which is fairly typical of TDEs. There is some short-timescale variability in the effective temperature that corresponds to the bumps in the light curve, which we showed earlier as being stronger at smaller wave-

lengths. We also fit a power law, $f_\lambda \propto \lambda^{-\alpha}$, to the host-subtracted *Swift* fluxes for each epoch. We find an average index of $\alpha = 2.35 \pm 0.35$, which is consistent with the $\alpha \simeq 2.3$ predicted for a standard thin accretion disc at UV/optical wavelengths (Shakura & Sunyaev 1973). In most epochs, the power-law fits are slightly better than the blackbody fits, usually with $\Delta\chi^2_\nu \simeq 1$. However, a $T \approx 2.5 \times 10^4$ K blackbody observed with the *Swift* filters is nearly indistinguishable from a power law with the same index, and so our data are still consistent with a single-temperature blackbody

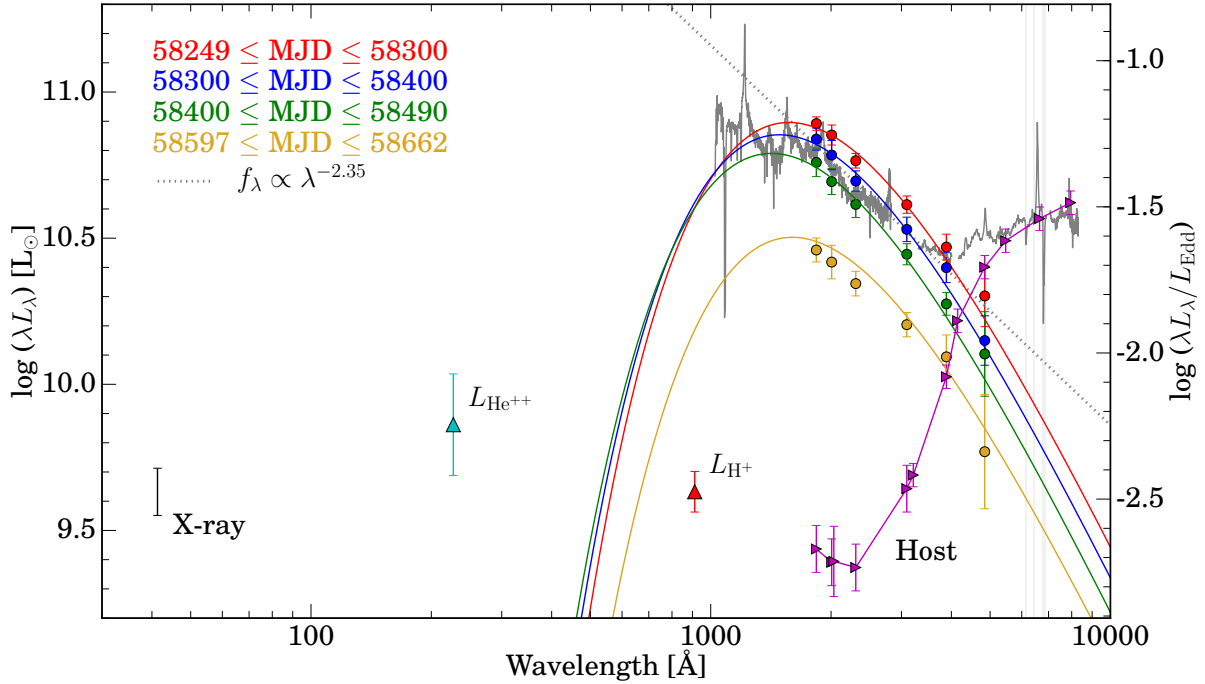


Figure 3. SED of ASASSN-18jd showing the average *Swift* UVOT data across a range of epochs as colored circles. The average blackbody fits (see Section 3) in these epoch ranges are shown as similarly colored lines. The average power-law fit (see Section 3) is shown as a dotted line. We show the FAST model of the host galaxy SED as magenta triangles (see Section 2.1) and the time-averaged optical and UV spectra (see Sections 5 and 6) as grey lines. We show the lower limits of the H- and He⁺-ionizing luminosities based on the average fluxes of the broad H α and He II λ 1640 features (see Sections 5.1 and 6) as red and cyan triangles. We show the mean 0.3–10 KeV X-ray luminosity of the *Swift* and *XMM-Newton* spectra (see Section 4) as a black circle.

spectrum. Moreover, with the addition of the UV spectra, we can see the SED break from a power law (see Figure 3) to track the blackbody SED model.

The bottom-left panel of Figure 4 shows the evolution of the effective radius, $R_{\text{eff}} = (L/4\pi\sigma T^4)^{1/2}$, of ASASSN-18jd and the TDEs. While the geometry is unlikely to be spherical, this should provide a reasonable estimate of the size of the optically thick, continuum-emitting region. The evolution of the radius is quite typical of TDEs, showing a monotonic decline in effective radius, but the evolution is slow compared to most TDEs. These R_{eff} are ~ 100 larger than the Schwarzschild radius, $R_{\text{Sch}} = 1.2^{+1.8}_{-0.7} \times 10^{13}$ cm, of the SMBH given our mass estimate. Finally, the bottom-right panel of Figure 4 compares the effective blackbody radius and the tidal radius of the SMBH for ASASSN-18jd and the other TDEs. We use our SMBH mass estimate of $M_{\text{BH}} = 10^{7.6} M_{\odot}$ for ASASSN-18jd and the SMBH masses from Wevers et al. (2017), Holoien et al. (2019a), and Wevers et al. (2019a) for the other TDEs, and we compute the tidal radius, $R_{\text{T}} = R_{*}(M_{\text{BH}}/M_{*})^{1/3}$, assuming a Sun-like star ($1 R_{\odot}, 1 M_{\odot}$). For ASASSN-18jd, $R_{\text{T}} = 2.4^{+0.8}_{-0.7} \times 10^{13}$ cm. While the effective radii shown in Figure 4 span nearly two orders of magnitude among the different TDEs, the ratio of $R_{\text{eff}}/R_{\text{T}}$ spans closer to one order of magnitude.

Integrating the blackbody luminosity over the span of our *Swift* observations in rest frame days, we find that the energy emitted as of the last observation is $E = 9.6^{+1.1}_{-0.6} \times 10^{51}$ erg. This corresponds to an accreted mass of $M_{\text{acc}} \simeq 0.054 M_{\odot}$, for an accretion efficiency of $\eta = 0.1$. This is larger than the accreted mass estimates of most TDEs over

similar timescales (Holoien et al. 2019a; van Velzen et al. 2019b). Recent TDEs studies have also shown that a significant amount of energy is radiated prior to peak brightness (Holoien et al. 2019a; Leloudas et al. 2019; Holoien et al. 2019b), meaning that a significant amount of energy was probably radiated prior to our first detection.

4 X-RAY DATA

In Figure 5, we compare the X-ray luminosity evolution as derived from the *Swift* XRT and *XMM-Newton* observations to the UV/optical luminosity evolution. Here the X-ray luminosity is estimated from the count rate using WebPIMMS⁷ assuming a $\Gamma = 1.75$ power law as derived from our X-ray spectra and the line-of-sight Galactic H I column density of $N_{\text{H}} = 2.71 \times 10^{20} \text{ cm}^{-2}$ from Kalberla et al. (2005).

The X-ray flux varies by roughly an order of magnitude ($\sim 10^{42.2} - 10^{43.2} \text{ erg s}^{-1}$) including an X-ray flare with a peak luminosity of $\sim 10^{43.7} \text{ erg s}^{-1}$ around +140 d (MJD 58354.2, ObsID:sw00010680024). By the time of the next *Swift* XRT observation, approximately 5 d later, the X-ray emission decreases to previously observed values. This flare occurs ~ 10 d prior to a peak in the UV/optical luminosity near +150 d (see Figures 2, 4, and 5). While the X-ray flare is quite short, only occurring over a few days,

⁷ <https://heasarc.gsfc.nasa.gov/cgi-bin/Tools/w3pimms/w3pimms.pl>

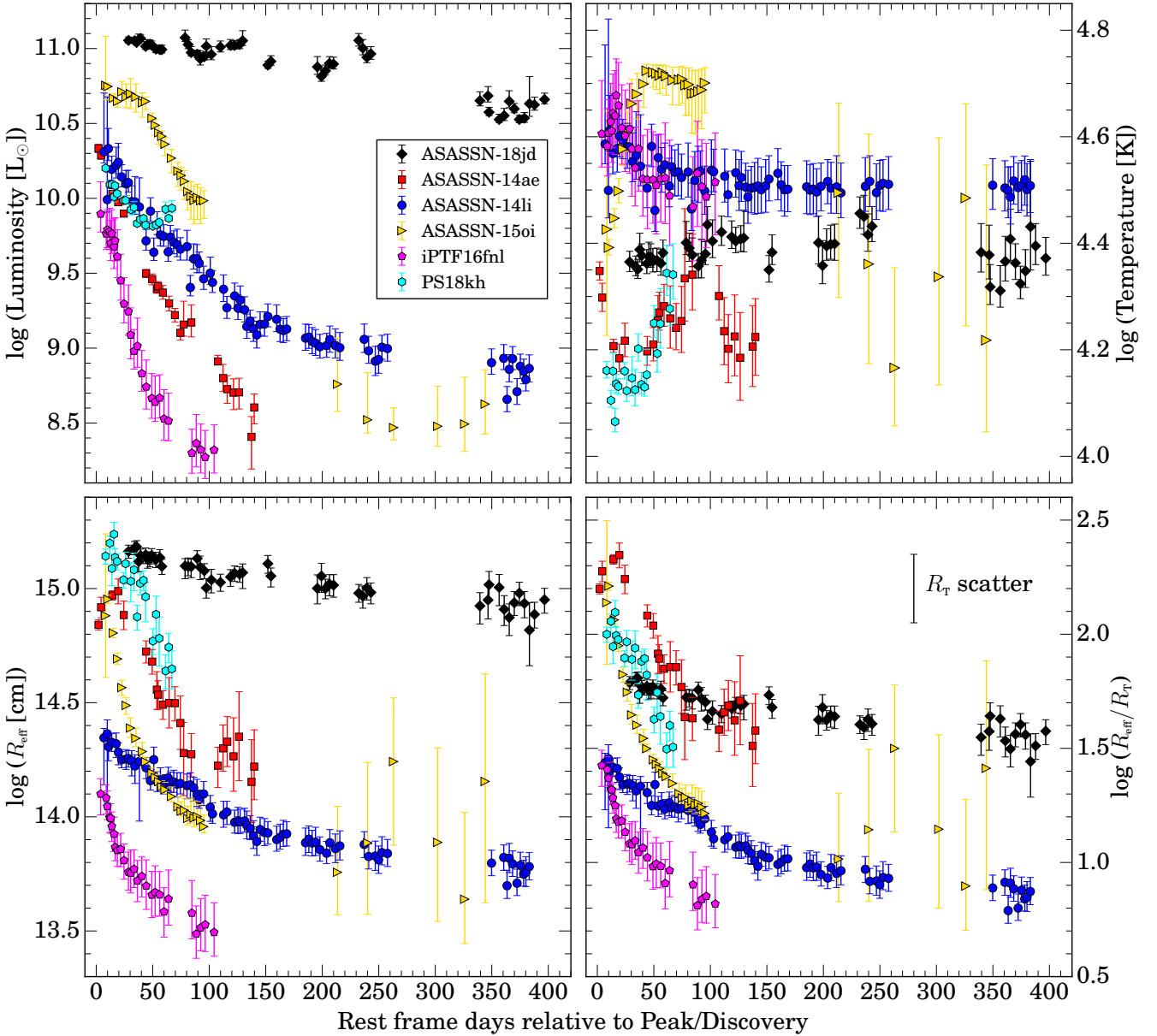


Figure 4. Evolution of ASASSN-18jd as compared to several well-studied TDEs based on blackbody fits to the *Swift* UVOT photometry. The events are color-coded as ASASSN-18jd (black diamonds), ASASSN-14ae (red squares), ASASSN-14li (blue circles), ASASSN-15oi (yellow triangles), iPTF16fnl (pink pentagons), and PS18kh (cyan hexagons). The top-left, top-right, and bottom-left panels show the luminosity, temperature, and effective radius (R_{eff}) evolution, respectively. The bottom-right panel normalizes R_{eff} to the tidal radius R_{T} of the host SMBH of the respective TDEs assuming a Sun-like star. Except for ASASSN-18jd and PS18kh (Holoien et al. 2019a), the SMBHs masses were taken from Wevers et al. (2017, 2019a). The error bar shows the average scatter of R_{T} caused by uncertainties in M_{BH} .

the UV flare near +150 d occurs on a longer timescale of some tens of days, implying that they are not necessarily related. Aside from the short flare, the X-ray light curve tends to follow a similar shallow decline to the optical/UV emission before fading completely after +275 d. We bin the observations after +275 d to get a $3\text{-}\sigma$ upper limit of $L_{\text{x,late}} < 1.1 \times 10^{42} \text{ erg s}^{-1}$.

In Figure 6, we show the evolution of the standard hardness ratio HR as a function of time. ASASSN-18jd shows significant X-ray color evolution with time, varying between

$HR = -0.75$ and 0. However, during the flare seen in the X-ray light curve around +140 d, the X-ray emission significantly softens, before hardening again after the flare ends. As the X-ray emission is well described by an absorbed blackbody and power-law component (see discussion below about the X-ray spectra), the softening during the X-ray flare may be the result of the blackbody component becoming stronger to create the increase in the soft X-ray flux. Large variations in hardness ratio are not seen in other well known X-ray emitting TDEs, such as ASASSN-14li and ASASSN-15oi,

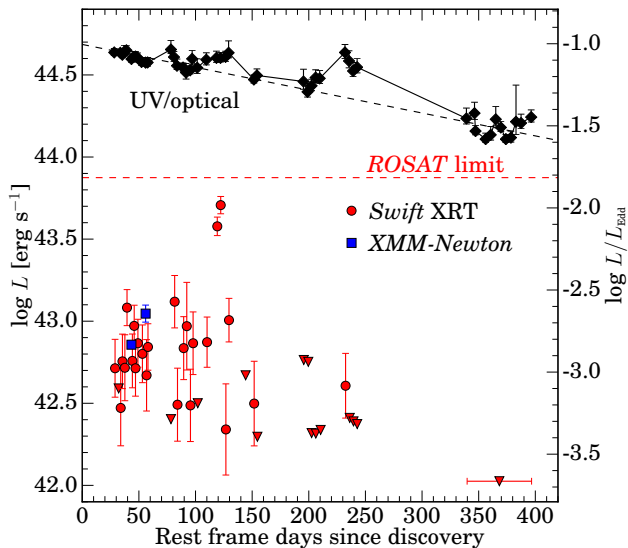


Figure 5. The evolution of the *Swift* XRT (red circles) and *XMM-Newton* (blue squares) 0.3–10 keV X-ray luminosities compared to the UV/optical blackbody luminosity (black diamonds) derived from the blackbody fits. Upper-limits derived from the *Swift* XRT data are plotted as red triangles. We show the *ROSAT* upper limit (red-dashed line) and the best fitting exponential-decay model for the blackbody luminosity (black-dashed line). We also plot the binned 3σ flux limit derived from the late-time *Swift* XRT epochs (MJD > 58500).

which tend to show very little variability in their hardness ratio with time (Auchettl et al. 2018; Holoien et al. 2018). This variation and softening as the flare peaks is similar to what is seen in AGNs, but in AGNs this softening is due to a steepening of the power-law component, whereas the blackbody component remains roughly constant (see Figure 4 from Auchettl et al. 2018). This is different from what we see in ASASSN-18jd, where the power-law index remains fixed and the blackbody component fluctuates.

We extract spectra from our two deep *XMM-Newton* observations and the merged *Swift* observations spanning the first and last ~ 200 d of our study. Due to the lack of X-ray emission at late times (see Figure 5), our second merged *Swift* spectrum does not have enough signal to characterize the emission and so we do not consider it further. In Figure 7, we show the unconvolved PN and MOS spectra from our two *XMM-Newton* observations and our merged *Swift* XRT spectrum with their best fit models and residuals. We find that all three spectra are well fit by an absorbed blackbody plus power-law model. Initially, the column density (N_H), blackbody temperature (kT), power-law index (Γ) and normalizations of each model were free parameters, but we find that N_H is unconstrained, so we fix it to the line-of-sight Galactic column density. We summarize the parameters derived from the X-ray spectra in Table 2. Fitting each spectrum with only one of the two components produces a significantly worse fit. Within the uncertainties, we find no evidence for changes in the power-law indices or blackbody temperatures between observations. The derived X-ray blackbody temperatures are consistent with those found for other X-ray bright TDEs, such as ASASSN-14li (Brown

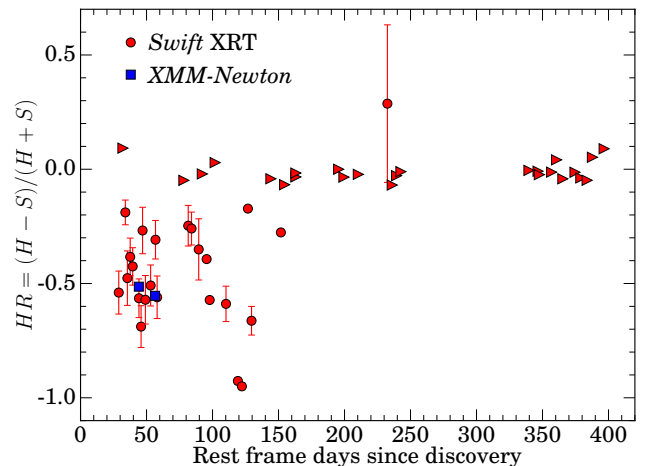


Figure 6. Evolution of the X-ray Hardness Ratio defined by $HR = (H - S)/(H + S)$ where H is the number of counts in the 2.0–10.0 keV energy range while S is the number of counts in the 0.3–2.0 keV energy range. We show the HR s derived from the individual *Swift* detections (red circles), the 3σ upper-limits (red triangles), and the two deep *XMM-Newton* observations (blue squares).

et al. 2017) and ASASSN-15oi (Gezari et al. 2017a; Holoien et al. 2018), and are on the low-temperature tail of blackbody temperatures found for AGNs (Reynolds 1997; Ricci et al. 2017). The observed power-law index is seen in both TDEs such as ASASSN-15oi (Gezari et al. 2017a; Holoien et al. 2018) and *Swift* J1644+57 (Burrows et al. 2011; Bloom et al. 2011) and in AGNs (Ricci et al. 2017). The mean and range of the total 0.3–10 keV luminosity derived from the three X-ray spectra are shown in Figure 3.

The luminosities of the blackbody and power-law components found for the two *XMM-Newton* observations are consistent given the uncertainties. However, our merged *Swift* spectrum for the first 200 d of emission, which includes the flare near +140 d, has a blackbody component that is approximately an order of magnitude more luminous, while the power-law component is slightly less luminous. The increase in the blackbody flux likely corresponds to an increase in the X-ray effective radius, as kT remains roughly constant. The apparent expansion of the X-ray emitting region during the flare is very different from the shrinking radius of the UV emitting region (see Figure 4).

The X-ray-derived blackbody radii of 3×10^{10} to 3×10^{11} cm are smaller than the Schwarzschild radius of the SMBH by a factor of roughly 30 to 300. These radii are also smaller than those found for the X-ray blackbodies of the TDEs ASASSN-14li and ASASSN-15oi (Brown et al. 2017; Holoien et al. 2018), which were both of order 10^{12} cm. Additionally, the X-ray blackbody radii of ASASSN-14li and ASASSN-15oi were 1–10 times larger than the associated SMBH Schwarzschild radii, rather than two orders of magnitude smaller. The X-ray blackbody radii for ASASSN-18jd are, however, similar to that of PS18kh, which also showed X-ray blackbody radii smaller than the predicted Schwarzschild radius by a factor of ~ 100 (van Velzen et al. 2019a). In AGNs, the blackbody component (also called the “soft-excess”) is thought to be created through other physical

Observation	Epoch [MJD]	Γ	kT [keV]	L_{pwl} [10^{43} erg s $^{-1}$]	L_{BB} [10^{43} erg s $^{-1}$]	R_{BB} [10^{10} cm]
<i>XMM-Newton</i> 1	58266.8	1.7 ± 0.1	0.08 ± 0.02	1.1 ± 0.5	0.31 ± 0.07	$9.0^{+34.8}_{-5.7}$
<i>XMM-Newton</i> 2	58280.6	1.7 ± 0.2	0.14 ± 0.04	1.4 ± 0.7	0.37 ± 0.06	$2.5^{+2.4}_{-1.0}$
Binned <i>Swift</i>	58249.8–58390.5	$1.7^{+0.4}_{-0.3}$	0.07 ± 0.01	0.54 ± 0.01	1.2 ± 0.3	31^{+19}_{-11}

Table 2. Parameters derived for the power-law and blackbody components of the three X-ray spectra. Luminosities are for the energy range of 0.3–10.0 keV.

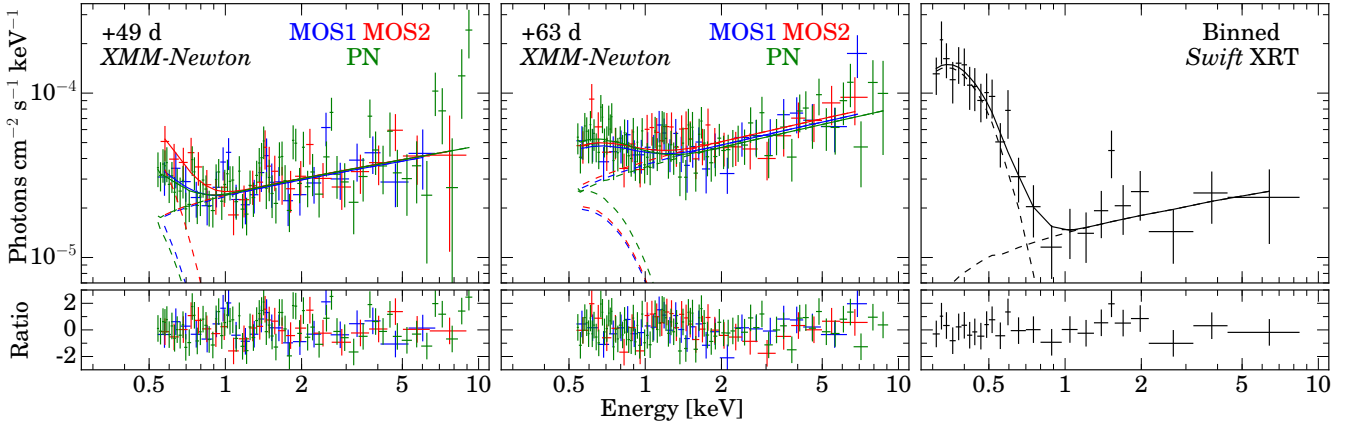


Figure 7. The two *XMM-Newton* spectra and the binned *Swift* XRT spectrum. For the *XMM-Newton* spectra, the red and blue data are from the two MOS cameras, and the green data are from the PN camera. The binned *Swift* spectrum only includes the first ~ 200 d of observations. The top panels show the data (crosses), the blackbody and power-law model fits (dashed lines), and the combined model fits (solid line). The bottom panels are the ratios between the model and the data.

processes like Comptonization and reprocessing, and thus a blackbody radius is not a meaningful quantity.

5 OPTICAL SPECTROSCOPY

The SALT, du Pont, Kast, and MODS spectra are presented in Figure 8. Because of the smaller wavelength coverage of the SNIFS spectra, they are presented separately in Figure 9. In both figures, prominent spectral features are labelled, and telluric bands are shaded. The most prominent features in the spectra are strong $H\alpha$, $H\beta$, and $H\gamma$ lines and a blue continuum. There are multiple features around 4600 \AA and a broad (FWHM $\sim 100 \text{ \AA}$) feature centered near 3430 \AA . There are also collisionally excited lines like [O II] $\lambda 3727$, [O III] $\lambda \lambda 4959, 5007$, [N II] $\lambda \lambda 6548, 83$, and [S II] $\lambda \lambda 6716, 31$ that are commonly seen in galaxy spectra. We can also see Ca II $\lambda \lambda 3934, 68$ and Mg I $\lambda \lambda 5173, 84$ absorption from the host and Na I $\lambda \lambda 5890, 96$ absorption from both our Galaxy and the host.

In Figure 10, we show the $H\alpha$ and $H\beta$ emission profiles. We decompose the $H\alpha$ profile into a sum of three narrow Gaussian profiles centered on $H\alpha$ and [N II] $\lambda \lambda 6548, 83$ and one broad Gaussian profile centered on $H\alpha$. We repeat this process for the $H\beta$ profiles in the du Pont, Kast, and MODS spectra (see Figure 8), using only one broad and one narrow Gaussian profile centered on $H\beta$. Because of the relatively low spectral resolution ($R \sim 300$) of the SALT spectra (see Figure 8), we are unable to decompose the Balmer line profiles. Similarly, we are unable to decompose the $H\beta$ profiles

in the SNIFS spectra due to noise (see Figure 9). The $H\gamma$ feature is different from the other Balmer features, showing a broad, flat-topped profile. Such $H\gamma$ profiles are sometimes seen in the spectra of broad-line AGNs. The most likely explanation for the irregular profile is contamination from nearby [O III] $\lambda 4363$, so we do not try to decompose the $H\gamma$ profile into narrow and broad components.

The narrow-line emission does not appear to change over time, and so it is likely coming from the host galaxy. Assuming the narrow-line emission is unrelated to the transient, we use the flux of the narrow $H\alpha$ component as a constant to scale the spectra across multiple epochs. We also measure the ratios of the narrow-line emission in the spectra, finding $\log([\text{N II}] \lambda 6583/\text{H}\alpha) = -0.3 \pm 0.1$, $\log([\text{O III}] \lambda 5007/\text{H}\beta) = 0.0 \pm 0.1$, $\log([\text{S II}] \lambda \lambda 6716, 32/\text{H}\alpha) = -0.7 \pm 0.1$. These ratios correspond to the “composite” region between the AGN-dominated and SF-dominated regions of the BPT diagrams (Kewley et al. 2001; Kauffmann et al. 2003). This fits with our understanding of the host as having only weak, if any, AGN activity before the transient. We measure the narrow-line $H\alpha$ emission to be $F_{\text{H}\alpha, \text{n}} = (6.0 \pm 0.7) \times 10^{-15} \text{ erg s}^{-1} \text{ cm}^{-2}$, corresponding to a luminosity $L_{\text{H}\alpha, \text{n}} = 2.2 \times 10^{41} \text{ erg s}^{-1}$. We also measure the [O II] $\lambda 3727$ emission to be $F_{[\text{O II}]} = (1.0 \pm 0.5) \times 10^{-15} \text{ erg s}^{-1} \text{ cm}^{-2}$, corresponding to a luminosity $L_{[\text{O II}]} = 3.7 \times 10^{40} \text{ erg s}^{-1}$. These luminosities correspond to SFR rates of $\text{SFR}_{\text{H}\alpha} = (1.8 \pm 0.2) \text{ M}_{\odot} \text{ yr}^{-1}$ and $\text{SFR}_{[\text{O II}]} = (0.5 \pm 0.2) \text{ M}_{\odot} \text{ yr}^{-1}$ (Kennicutt 1998). These SFR rates are reasonably consistent with the estimate of $\text{SFR} = 0.6^{+0.1}_{-0.3} \text{ M}_{\odot} \text{ yr}^{-1}$ found from the FAST SED mod-

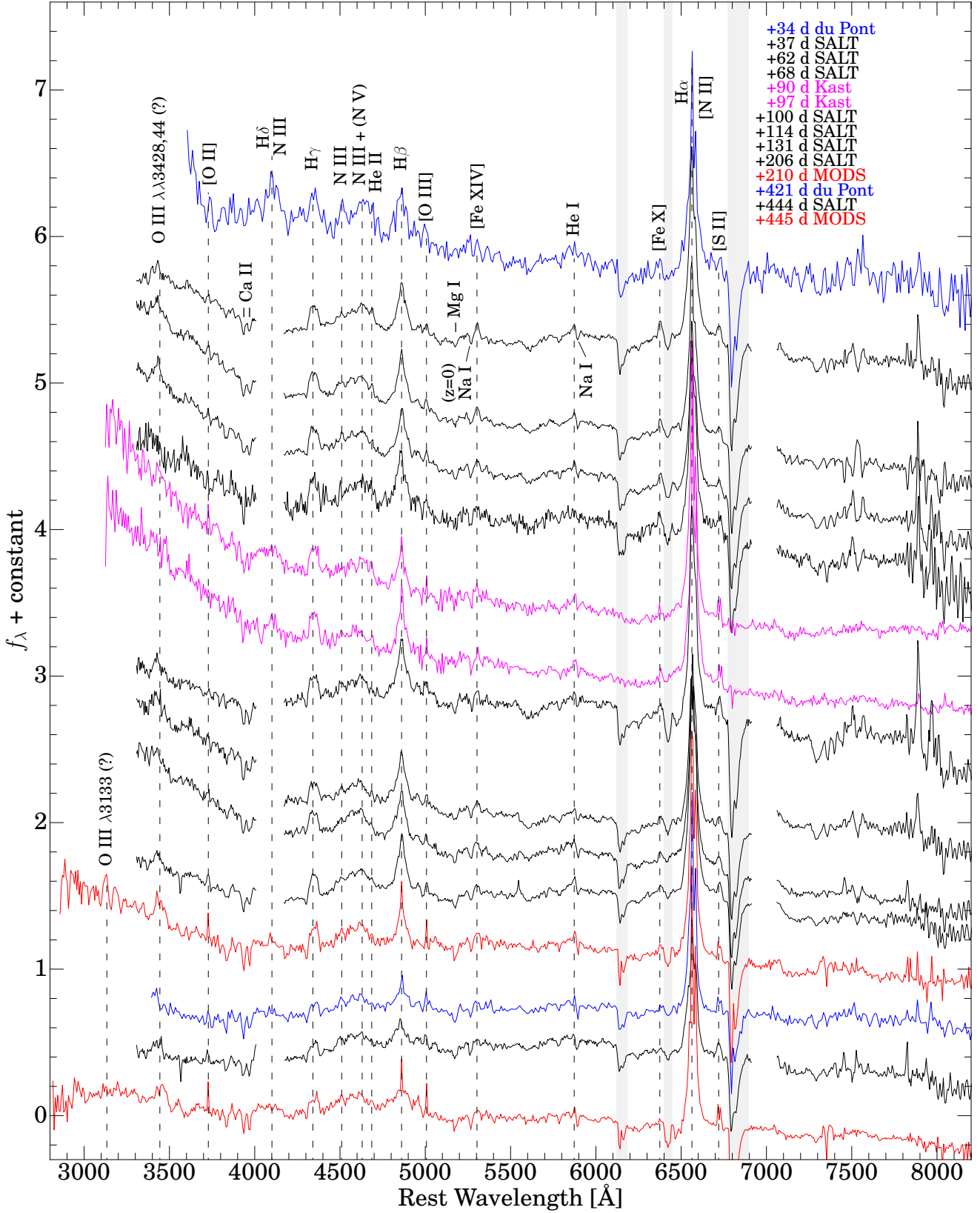


Figure 8. The du Pont (blue), SALT (black), Kast (magenta), and MODS (red) spectra. Prominent spectral features are labelled, and regions strongly affected by telluric absorption are shaded. The du Pont, SALT, Kast, and MODS spectra were smoothed with 10, 5, 7, and 7 Å-wide bins, respectively. The gaps in the SALT spectra are due to the spectrograph’s design.

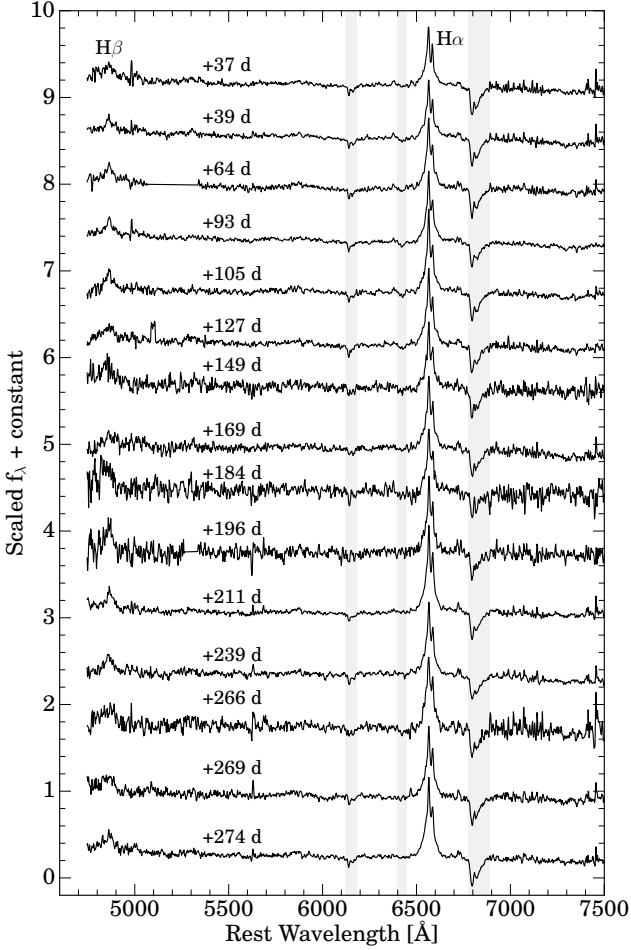


Figure 9. Multi-epoch SNIFS spectra of ASASSN-18jd. Regions strongly affected by telluric absorption are shaded.

els in Section 2.1, suggesting that much of the narrow-line emission is due to star formation.

5.1 Balmer features

The evolution of the flux and FWHM of the broad $H\alpha$ and $H\beta$ features are shown in Figure 11. To estimate the uncertainties, we resample the spectra with bootstrapping methods. In each trial a spectral data point is randomly sampled n_i times. For $n_i > 0$, we reduce the error to $\sigma_i/\sqrt{n_i}$, while for $n_i = 0$, we double the error. We do this 100 times and use the mean and dispersion of the results for Figure 11. After excluding the points with the largest error bars, the broad $H\alpha$ features have an average FWHM of $3250 \pm 350 \text{ km s}^{-1}$. In the du Pont spectra, the broad $H\beta$ features, which are relatively noisy, have FWHM of $5900 \pm 1000 \text{ km s}^{-1}$ and $5900 \pm 400 \text{ km s}^{-1}$. In the Kast spectra, the $H\beta$ features have similar FWHMs of $3600 \pm 400 \text{ km s}^{-1}$ and $4100 \pm 300 \text{ km s}^{-1}$. The MODS spectra yield very different $H\beta$ FWHMs of $3200 \pm 200 \text{ km s}^{-1}$ and $7000 \pm 200 \text{ km s}^{-1}$. This last measurement is peculiarly large, especially considering the fact that the $H\alpha$ FWHM is not anywhere near as large. While Figure 11 may appear to show an inverse correlation between the flux and FWHM of the broad $H\alpha$ feature, the three points

with larger flux and smaller FWHM values are also from the noisiest spectra. Additionally, the $H\beta$ feature appears to show the opposite trend. The most likely explanation is that these features are roughly constant over time, and the fluctuations seen in Figure 11 are dominated by noise.

Generally, the Balmer features of H-rich TDEs fade and become narrower as the continuum fades. ASASSN-14li, for example, showed a roughly linear correlation between the continuum and the $H\alpha$ luminosities and line width while fading (Holoien et al. 2016a; Brown et al. 2017). By contrast, the Balmer features of AGNs become fainter ($\propto L^{0.5}$) but broader ($\propto L^{-0.25}$) as the continuum luminosity (L) fades (Korista & Goad 2004; Peterson et al. 2004; Denney et al. 2009). ASASSN-18jd shows neither trend despite the continuum having faded by a factor 3–5 by the time of the last epoch where spectra were taken.

We use the flux of the broad component of the $H\alpha$ emission to estimate the unobserved H-ionizing luminosity. The average broad $H\alpha$ line flux of $F_{H\alpha,b} = (2.5 \pm 0.4) \times 10^{-14} \text{ erg s}^{-1} \text{ cm}^{-2}$ corresponds to an $H\alpha$ luminosity of $L_{H\alpha,b} = 9.4 \times 10^{41} \text{ erg s}^{-1}$, which implies a minimum H-ionizing luminosity of $L_{H^+} = 1.6 \times 10^{43} \text{ erg s}^{-1}$, assuming Case B recombination. While this is comparable to the H-ionizing luminosity of other H-rich TDEs (Brown et al. 2017), it is several orders of magnitude smaller than our predicted blackbody luminosity at the 912 Å Lyman continuum break from the UV/optical blackbody fits shown in Figure 3. This implies a small covering fraction for the line emitting gas, which is also true in the BLRs of AGNs. If we assume the $R_{\text{BLR}}-L$ relationship from Bentz et al. (2009) holds, then the BLR radius has a range of $R_{\text{BLR}} \sim (5 \pm 2) \times 10^{14} \text{ cm}$, which places the material outside the tidal disruption radius for a Sun-like star, yet inside the photospheric radius estimated from the blackbody fits. Similarly, if we interpret the line widths as an estimate of the escape velocity using our average $H\alpha$ width of $\text{FWHM} = 3250 \text{ km s}^{-1}$, we get a radius for the Balmer emission of $R_{H\alpha,esc} \sim 1 \times 10^{17} \text{ cm}$, which is outside the photospheric radius.

5.2 He and metal lines

The series of features around 4600 Å show multiple peaks at roughly 4510, 4570, 4635, and 4686 Å. These features are visible in Figure 8 and highlighted in Figure 12. The last of these features is easily attributed to He II $\lambda 4686$, which is a common feature in TDE spectra (e.g., Arcavi et al. 2014). The other features (and/or features at similar wavelengths) are also seen in some TDE spectra (see, e.g., Leloudas et al. 2019). A possible origin of these features is a blend of highly ionized N lines that are seen in Wolf-Rayet (WR) stars (see, e.g., Crowther 2007), in particular N III $\lambda 4510$, N V $\lambda 4610$, and N III $\lambda\lambda 4634,40$. Alternatively, this emission could be due to Fe II, which is commonly seen in AGN spectra and has been recently identified in the spectra of the TDEs ASASSN-15oi and ASASSN-18ul (Wevers et al. 2019b). Commonly-used Fe II templates (e.g., Kovačević et al. 2010) list the brightest lines in this wavelength regime as $\lambda 4418$, $\lambda 4523$, $\lambda 4549$, $\lambda 4583$, and $\lambda 4629$, where the last line is actually a blend of two lines whose relative strengths vary. N III-V seems the more likely contributors to the emission profile, although some features line up with Fe II lines, and there are no strong

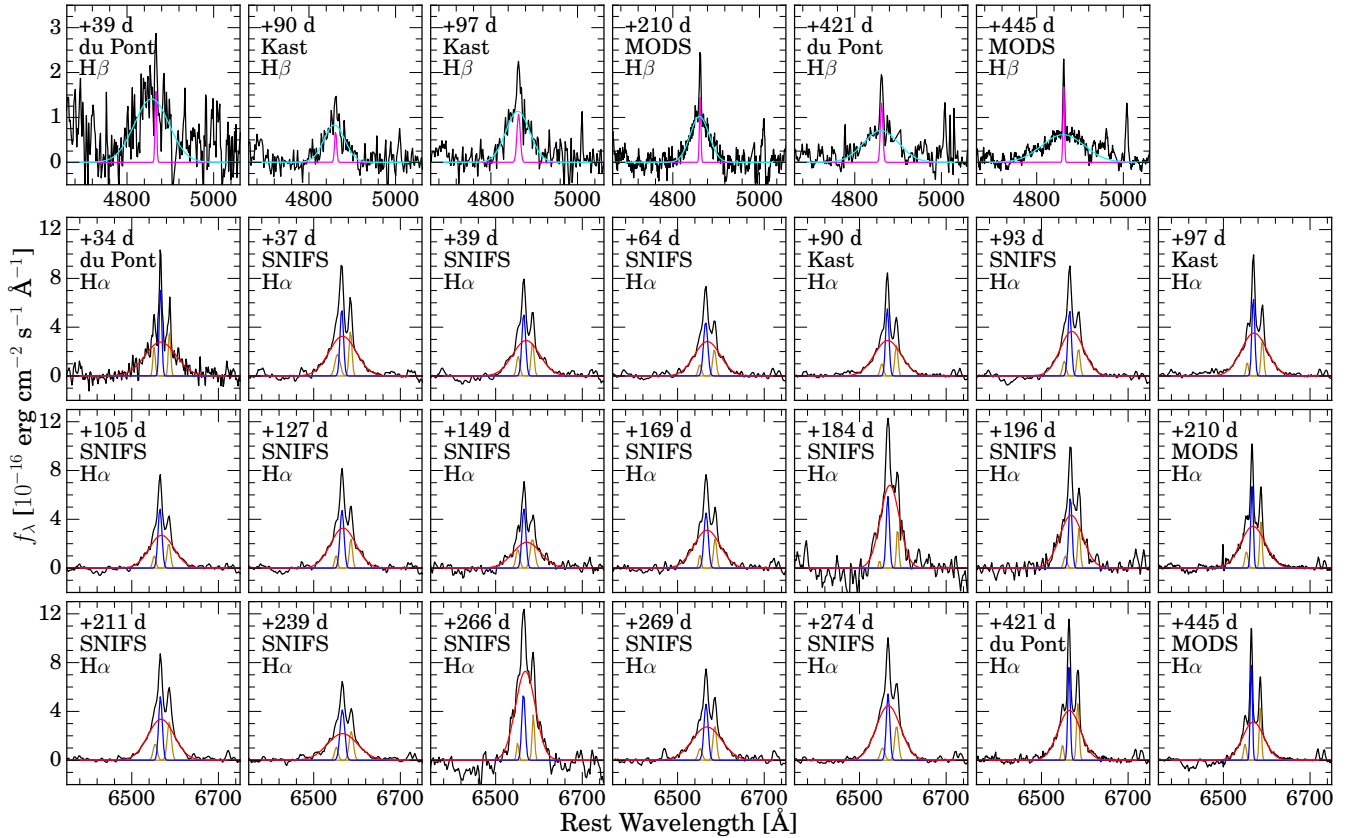


Figure 10. Continuum-subtracted $H\alpha$ and $H\beta$ profiles from the optical spectra. For the $H\alpha$ profiles, the black lines show the spectra, and the blue, yellow, and red lines show the best fitting Gaussian profiles for the narrow $H\alpha$, $[N\text{II}] \lambda\lambda 6548, 83$, and broad $H\alpha$ components, respectively. For the $H\beta$ profiles, the black lines show the spectra, and the magenta and cyan lines show the best fitting Gaussian profiles for the narrow and broad $H\beta$ components, respectively. The spectra were scaled to one another by holding the integrated flux of the narrow $H\alpha$ emission constant. The spectra are labelled by date and source.

$N\text{III-V}$ lines near the feature at 4570\AA , so $N\text{III-V}$ cannot be the sole source of emission in this wavelength region.

In addition to the features around 4600\AA , we can see a prominent emission feature near $H\delta \lambda 4101$ in the +34 d, +90 d, and +97 d spectra. In the +34 d spectrum, this feature appears stronger than $H\gamma$, implying that the emission at 4100\AA must be contaminated by emission from another source. The most likely line is $N\text{III} \lambda 4100$, a commonly observed line in WR spectra that is of equal strength to $N\text{III} \lambda 4640$ and that has been identified in other TDE spectra (Blagorodnova et al. 2019; Leloudas et al. 2019).

As we see in Figure 12, the $\text{He II} \lambda 4686$ line appears to get weaker over time compared to the nearby $N\text{III} \lambda 4640$. At earlier times, the He II emission is nearly as strong as the $N\text{III}$, whereas at later times, the He II line is only barely visible. For comparison, ASASSN-14li and ASASSN-18pg showed the opposite behavior, where the $N\text{III}$ line started brighter and became fainter than the He II line (Holoien et al. 2016a; Leloudas et al. 2019). Additionally, the $H\delta \lambda 4101 + N\text{III} \lambda 4100$ emission feature appears quite prominent and quite broad ($\text{FWHM} \sim 100\text{\AA}$) in the +34 d spectrum, and it appears fainter in the +90 d and +97 d spectra. In the +210 d spectrum, the emission is both fainter and narrower, and in the +421 d and the +445 d spectra, the feature does not appear at all (see Figure 8).

Throughout the epochs, we can see a broad featured centered near 3430\AA . In the +210 d MODS spectrum, we can see a slightly brighter yet narrower bump centered near 3130\AA . Recent studies of TDE spectra (Blagorodnova et al. 2019; Leloudas et al. 2019) have identified similar features at these wavelengths as $\text{O III} \lambda 3133$ and $\text{O III} \lambda\lambda 3428, 44$. These studies have also proposed that these O III emission lines, as well as the $N\text{III}$ emission lines at $N\text{III} \lambda 4100$ and $N\text{III} \lambda 4640$, are due to Bowen Fluorescence (BF) with $\text{He II} \lambda 303.78$ emission (Bowen 1934). However, there are some problems with this interpretation. BF would not produce any $N\text{III}$ lines in this region besides $N\text{III} \lambda\lambda 4097, 4103$ and $N\text{III} \lambda\lambda 4634, 40$ (McClintock et al. 1975; Netzer et al. 1985; Selvelli et al. 2007). This is in conflict with our identification of $N\text{III} \lambda 4510$. Additionally, $\text{O III} \lambda 3133$ should be roughly 3 times stronger than $\text{O III} \lambda 3444$ (McClintock et al. 1975; Netzer et al. 1985; Liu et al. 1993; Kastner & Bhatia 1996; Selvelli et al. 2007). This is not the case in our spectra, though the exact strengths are difficult to estimate because these are broad features and could be blended with other lines, such as $[\text{Ne V}] \lambda 3426$. However, an additional problem arises from the fact that in the +445 d MODS spectrum, the $\text{O III} \lambda 3133$ feature is barely visible if at all, whereas the $\text{O III} \lambda 3444$ feature is still quite prominent. These inconsistencies are difficult to explain with BF, so it may be that

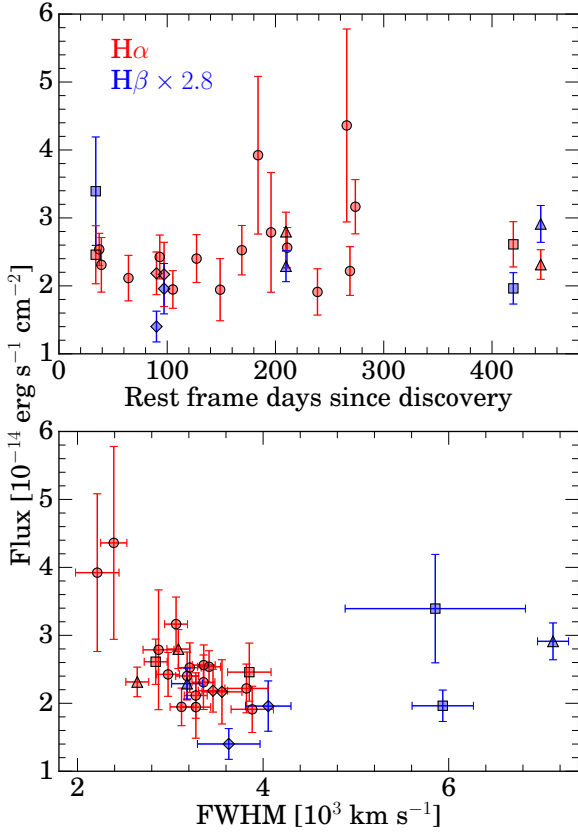


Figure 11. Top: The evolution of the broad H α and H β flux over time. The error-bars are 1σ . The H β fluxes are scaled by a factor of 2.8, the expected ratio of H α /H β for recombination. **Bottom:** The dependence of the flux on the FWHM for the broad H α and H β profiles. The SNIFS, du Pont, Kast, and MODS spectra are represented by circles, boxes, diamonds, and triangles, respectively.

BF is not responsible for the emission at 3430 Å and 3430 Å or for the N III emission in ASASSN-18jd.

We observe an emission line centered at 6375 Å that is best seen in the early-time optical spectra. This may be [Fe X] λ 6375, a coronal (high-ionization, forbidden) line often seen in AGN spectra. This identification may be problematic because of its closeness to the telluric band at 7186 Å (host rest-frame \sim 6420 Å). However, this feature also appears to fade over time, providing evidence that the feature is in fact real. There also appears to be a feature around 5300 Å that might be due to [Fe XIV] λ 5303, another coronal emission line seen in AGNs, but this region is affected by Milky Way absorption from Na I λ 5890,96 (host rest-frame \sim 5260 Å). While these lines are seen in AGNs, notably Narrow Line Seyfert 1s (NLSy1s), these lines are usually accompanied by lower-level ionization lines like [Fe VII] λ 6088 and are much weaker than emission from [O III] λ 5007. When these lines are brightest in ASASSN-18jd’s spectra, [Fe VII] λ 6088 is not present, and [Fe X] λ 6375 is roughly equivalent in strength to [O III] λ 5007, implying that these lines are not attributable to “normal” AGN or NLSy1 activity. These lines are indicative of strong soft X-ray flux, as Fe X and Fe XIV have ionization potentials of 234 eV and 361 eV, respectively. The transient nature of the lines, especially [Fe X] λ 6375, implies

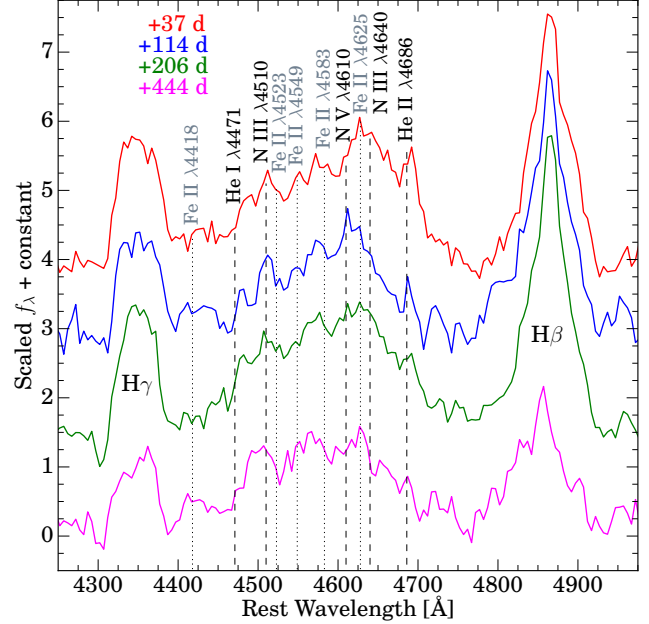


Figure 12. Multi-epoch SALT spectra of the emission features near 4600 Å. Dashed lines denote He and potential N III-V lines present in the spectra, and dotted lines mark potential Fe II lines that are observed in AGNs and some TDEs (Wevers et al. 2019b). Fe II lines are taken from Kovačević et al. (2010). Over time, the He II λ 4686 emission appears to get weaker with respect to the bluer N III emission.

that they are associated with the transient X-ray flux of ASASSN-18jd. Other studies have found similar, transient coronal Fe lines in galaxies with faint or no AGN activity (Komossa et al. 2009; Wang et al. 2011, 2012). These galaxies were dubbed Extreme Coronal Line Emitters (ECLEs) (Wang et al. 2012), and it was proposed that the soft X-ray flux required to generate these lines could originate from TDEs.

6 UV SPECTROSCOPY

We present the six epochs of *HST*/STIS UV spectra of ASASSN-18jd in Figure 13. There is a \sim 20–25 per cent difference between STIS and *Swift* fluxes for concurrent epochs, which is likely explained by slit losses and the large widths of the *Swift* filters. We show the scaled *Swift* fluxes and fitted blackbody continua in Figure 13 along with the STIS spectra to show the strengths of line features relative to the continuum. The most prominent emission features seen for all the epochs are Ly α , N V λ 1240, Si IV λ 1394,1403, C IV λ 1550, He II λ 1640, and C III] λ 1909, as well as faint bumps attributable to O I λ 1302 and N III] λ 1750. There are absorption features at local-rest-frame Ly α , Si II λ 1260, O I λ 1302/Si II λ 1304, C II λ 1335, Si II λ 1527, C IV λ 1550, and Mg II λ 2800. There also appears to be a double-peaked feature around 2800 Å that is most likely Mg II λ 2800, though it is difficult to be certain because the feature is close to the detector’s edge.

The lack of strong N III-V features is in conflict with our identification of the features at 4100 Å and near 4600 Å as

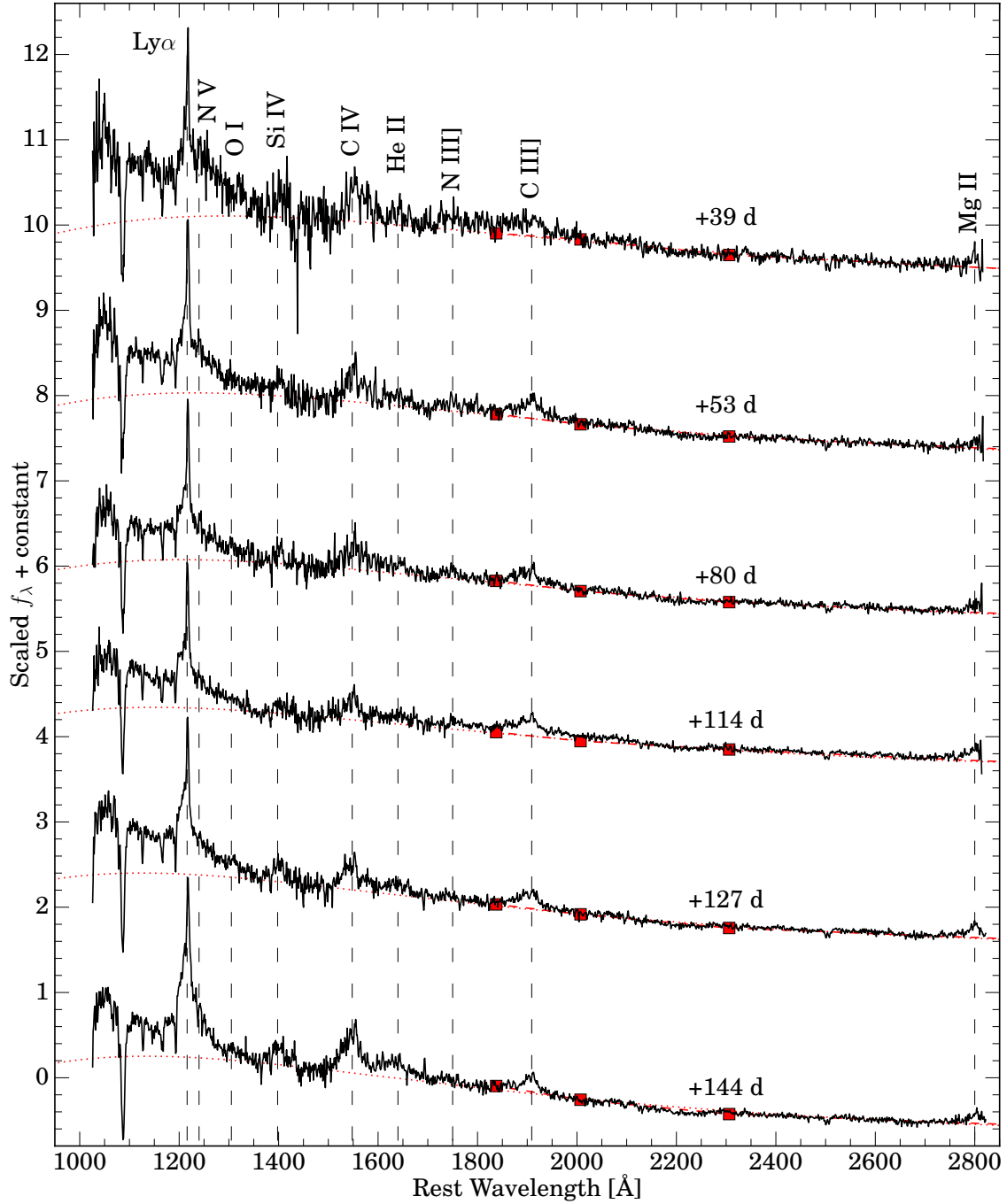


Figure 13. Multi-epoch UV spectra of ASASSN-18jd from *HST*/STIS. The spectra were extinction corrected and smoothed with 1 Å-wide bins. Prominent spectral features are labelled. All absorption features are due to telluric and Galactic absorption and not associated with the transient. The *Swift* fluxes (red squares) that were observed in roughly concurrent epochs are scaled in the plot to match the flux values of the spectra at the filters’ center wavelengths. Also plotted are the (scaled) blackbody models (dashed-red lines) derived from the *Swift* fluxes. The absolute values differ by 20–25 per cent.

N III-v emission. Most notable is the absence of N IV] $\lambda 1486$. Since the critical density of N IV] $\lambda 1486$ is of the same order of magnitude as the critical density for C III] $\lambda 1909$, with $n_{\text{crit}} \sim 10^9\text{--}10^{10} \text{ cm}^{-3}$, the lack of N IV] $\lambda 1486$ is likely not a consequence of having a particular density for the line-emitting gas. This lack of N III-v emission is not an issue if the optical N III lines are due to BF, which does not produce

strong N III-v lines in the NUV or FUV (McClintock et al. 1975; Netzer et al. 1985; Liu et al. 1993; Kastner & Bhatia 1996; Selvelli et al. 2007).

We trace the evolution of the Ly α feature across epochs using the same method that we use for fitting the H α profiles. We find that the feature can be roughly decomposed into narrow (FWHM $\sim 1000 \text{ km s}^{-1}$) and broad (FWHM

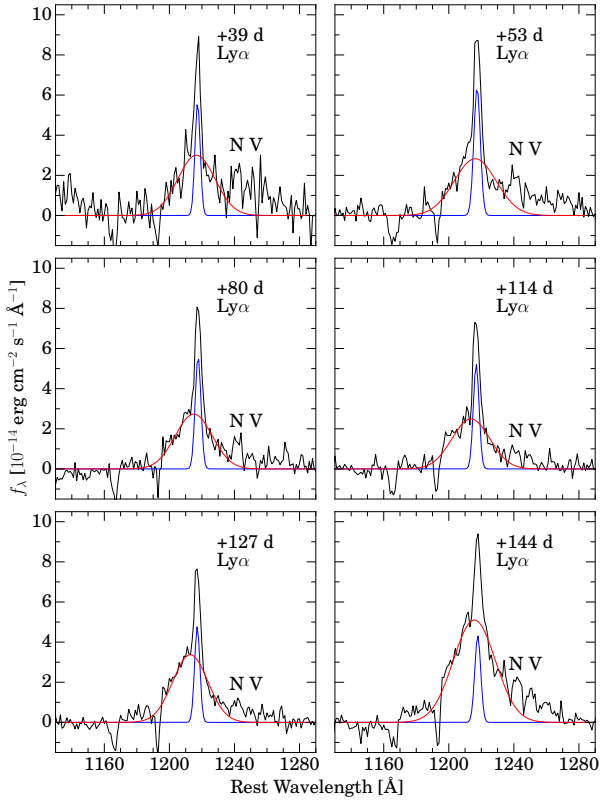


Figure 14. Continuum-subtracted Ly α profiles from the STIS spectra. The black lines are the 1-Å-bin smoothed spectra, and the blue and red lines show the best fitting Gaussian profiles for the narrow Ly α and broad Ly α components, respectively. The N v λ 1240 emission is also labelled.

$\sim 7000 \text{ km s}^{-1}$) components. Additionally, we find that the broad component becomes brighter during the last epoch of observation. This is true whether or not we hold the narrow component fixed in flux. The continuum-subtracted Ly α features and the fits associated with them are presented in Figure 14. Because Ly α is very sensitive to changes in opacity and optical depth, the change in this line profile over time implies some dynamical changes in the system over time that are not discernible from the Balmer lines. The maximum broad Ly α flux taken from the last epoch is $F_{\text{Ly}\alpha} = (1.7 \pm 0.1) \times 10^{-13} \text{ erg s}^{-1} \text{ cm}^{-2}$, whereas for the other five epochs, the average flux is $F_{\text{Ly}\alpha} = (8.4 \pm 2.3) \times 10^{-14} \text{ erg s}^{-1} \text{ cm}^{-2}$.

The broad He II λ 1640 feature can be used to estimate the He $^+$ -ionizing luminosity. We get an integrated flux of $F_{1640 \text{ \AA}} \simeq (5 \pm 2) \times 10^{-14} \text{ erg s}^{-1} \text{ cm}^{-2}$, corresponding to a luminosity $L_{1640 \text{ \AA}} = 2.5 \times 10^{42} \text{ erg s}^{-1}$. Assuming Case B recombination and $T = 2 \times 10^4 \text{ K}$ gas, this luminosity implies a minimum He $^+$ -ionizing luminosity of $L_{\text{He}^{++}} = 2.8 \times 10^{43} \text{ erg s}^{-1}$. We compare this estimate of the He $^+$ -ionizing luminosity to the UV/optical blackbody luminosity in Figure 3. This luminosity is the same order of magnitude as the H-ionizing flux, yet it is significantly higher than the predicted blackbody luminosity at the He $^+$ -ionizing edge at 227 Å. This implies that there is a significant amount of EUV photons that are being generated by a currently-unseen radiation source.

Aside from the changes in Ly α and some apparent fluc-

tuations of N v λ 1240, the UV spectra of ASASSN-18jd do not appear to change with time. This is in contrast to the optical spectra, where He II λ 4686, N III λ 4100 and [Fe x] λ 6375 weaken over time, albeit over longer timescales than the differences between the *HST* epochs.

7 DISCUSSION

ASASSN-18jd is a unique event among transients and shares properties with optically-detected TDEs and with AGNs. We compare the optical and UV spectra of ASASSN-18jd to well-studied TDEs, other nuclear transients, and objects with similar spectra in Figures 15 and 16. In Figure 15, we compare two early-time optical spectra of ASASSN-18jd to known TDEs (Holoien et al. 2014, 2016a,b; Hung et al. 2017; Blagorodnova et al. 2019; Hung et al. 2019), as well as the composite quasar spectrum from Vanden Berk et al. (2001), an early-time spectrum of the TDE candidate PS16dtm (Blanchard et al. 2017), an early-time spectrum of the changing-look LINER ZTF18aa:jupnt/AT 2018dyk (Frederick et al. 2019), and the spectrum of a WR star with strong He II and N III-v features (Yaron & Gal-Yam 2012). In Figure 16, we compare a UV spectrum of ASASSN-18jd to TDEs with published UV spectra (Cenko et al. 2016; Brown et al. 2018; Blagorodnova et al. 2019; Hung et al. 2019), ZTF18aa:jupnt (Frederick et al. 2019), the composite quasar spectrum from Vanden Berk et al. (2001), and an “N-rich” quasar spectrum (Batra & Baldwin 2014).

7.1 ASASSN-18jd as a TDE

The SED of ASASSN-18jd is TDE-like, with a strong blue continuum that is reasonably-well fit by a blackbody with temperature $T \simeq 2.5 \times 10^4 \text{ K}$. With a maximum observed luminosity of $L_{\text{max}} = 4.5_{-0.3}^{+0.6} \times 10^{44} \text{ erg s}^{-1}$, ASASSN-18jd would be one of the most luminous optically-discovered TDEs to date, and its host galaxy would be one of the most massive TDE host galaxies. Our SMBH mass estimate of $\log M_{\text{BH}}/M_{\odot} = 7.6 \pm 0.4$ is one of the largest masses for a SMBH associated with an observed TDE (Wevers et al. 2017, 2019a).

Empirically, it has been suggested that the UV/optical fading timescale increases with SMBH mass (Blagorodnova et al. 2017; Wevers et al. 2017; van Velzen et al. 2019b). ASASSN-18jd has a decay rate of 3.3 mmag d $^{-1}$ in the *Swift* UVW2 and UVW1 filters. In these terms, the most similar TDE is GALEX D3-13, which has a SMBH mass estimate of $\log M_{\text{BH}}/M_{\odot} = 7.36 \pm 0.44$ and a decay rate of 2.6 \pm 0.2 mmag d $^{-1}$ (Wevers et al. 2017). However, GALEX D3-13 has a very sparsely-sampled light curve compared to ASASSN-18jd, so it is unclear how well the two decay rates match.

The luminosity evolution of ASASSN-18jd is different from “normal” TDEs in that it does not smoothly decline. There appear to be multiple bumps in the light curve where the luminosity returns to near maximum values, similar to that seen from highly variable AGNs. By comparison, most TDEs with well-sampled UV/optical light curves show only smooth, monotonic fading. Some recently discovered TDEs have shown deviations from monotonic fading: ASASSN-18ul showed a light curve plateau \sim 40 d after peak bright-

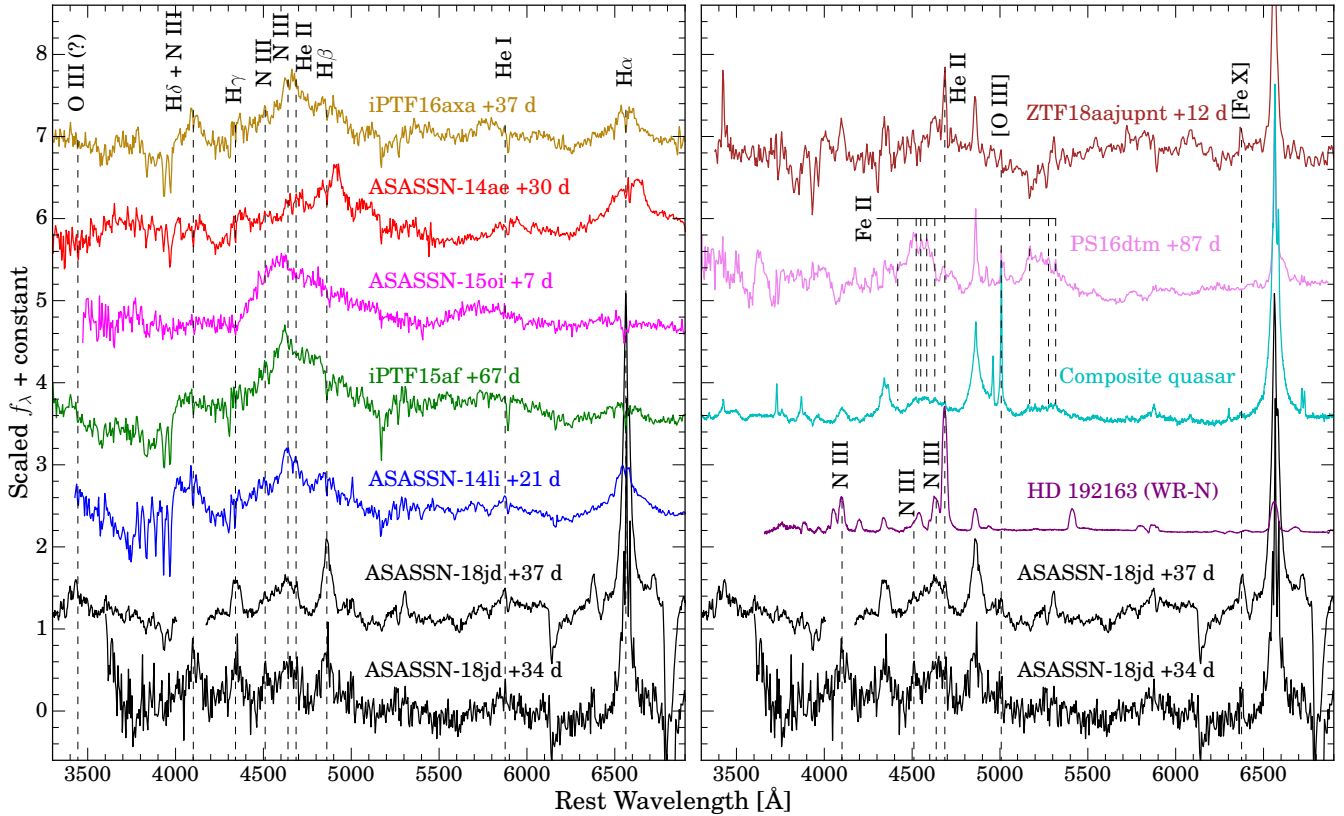


Figure 15. **Left:** Early-time optical spectra of ASASSN-18jd compared to known TDEs. The spectra are not host-subtracted. **Right:** Early-time optical spectra compared to a composite quasar spectrum, the TDE candidate PS16dtm, the changing-look LINER ZTF18aajupnt, and a N-type WR star. We approximated and subtracted the continuum of each spectra in order to compare spectral emission features, which are labelled.

ness (Wevers et al. 2019b) and ASASSN-19bt showed a short flare before reaching peak brightness (Holoien et al. 2019b). In a more extreme example, PS18kh showed a UV re-brightening ~ 50 d after peak (Holoien et al. 2019a) and then, after a seasonal gap due Sun constraints, appeared to return to near-peak luminosity (van Velzen et al. 2019a). However, these deviations from monotonic fading were still “smooth”, with little short-timescale variation, which is qualitatively different from the bumpiness in the light curve of ASASSN-18jd.

As seen in Figure 15, the optical spectra of ASASSN-18jd are different from the spectra of other TDEs. The Balmer features of ASASSN-18jd are narrower than those in TDEs like ASASSN-14ae, iPTF16axa, and iPTF16fnl (Holoien et al. 2014; Hung et al. 2017; Blagorodnova et al. 2017). The widths of the Balmer features are similar to those of ASASSN-14li, which had a maximum $H\alpha$ FWHM of ~ 3000 km s^{-1} (Holoien et al. 2016a). However, the Balmer features of ASASSN-14li showed a clear evolution, becoming dimmer and narrower as the continuum faded (Holoien et al. 2016a; Brown et al. 2017), whereas the Balmer features of ASASSN-18jd do not show any coherent evolution. ASASSN-14li was also discovered after a seasonal gap in ASAS-SN coverage and as it was fading, and thus its emission lines were probably broader than ~ 3000 km s^{-1} closer to its actual peak brightness.

With the exception of ASASSN-14li, the H-ionizing luminosity estimated from the $H\alpha$ flux for other TDEs is usually greater than the predicted blackbody luminosity. This could be related to the lack of evolution in the Balmer features of ASASSN-18jd. Generally, in both TDEs and reverberation mapped AGNs, the Balmer line fluxes drop with the continuum luminosity L . For TDEs, this is usually $L_{H\alpha} \propto L$ (Brown et al. 2017), whereas for AGNs, this is usually $L_{H\alpha} \propto L^{0.5}$ (Korista & Goad 2004). This is not the case for ASASSN-18jd, where the Balmer line fluxes remained roughly constant while the continuum luminosity dropped. A possible explanation is that the broad line emission could be limited by the amount of broad line gas rather than the luminosity needed to ionize it. In this “matter bounded” scenario, the line luminosity becomes insensitive to changes in the ionizing continuum luminosity, which would also explain the lack of evolution in the FWHM of the Balmer lines. Regardless, the relatively weak dependence of Balmer flux to continuum seen in ASASSN-18jd is more similar to AGN activity than emission from TDEs.

The optical spectra and SED evolution of ASASSN-18jd resembles that of the transient PS16dtm, claimed to be a TDE in a known NLSy1. PS16dtm brightened rapidly (~ 50 d), faded slowly, and exhibited a transient blue continuum and variable, strong Fe II line emission. While PS16dtm showed an increase in the UV and optical flux, the upper-

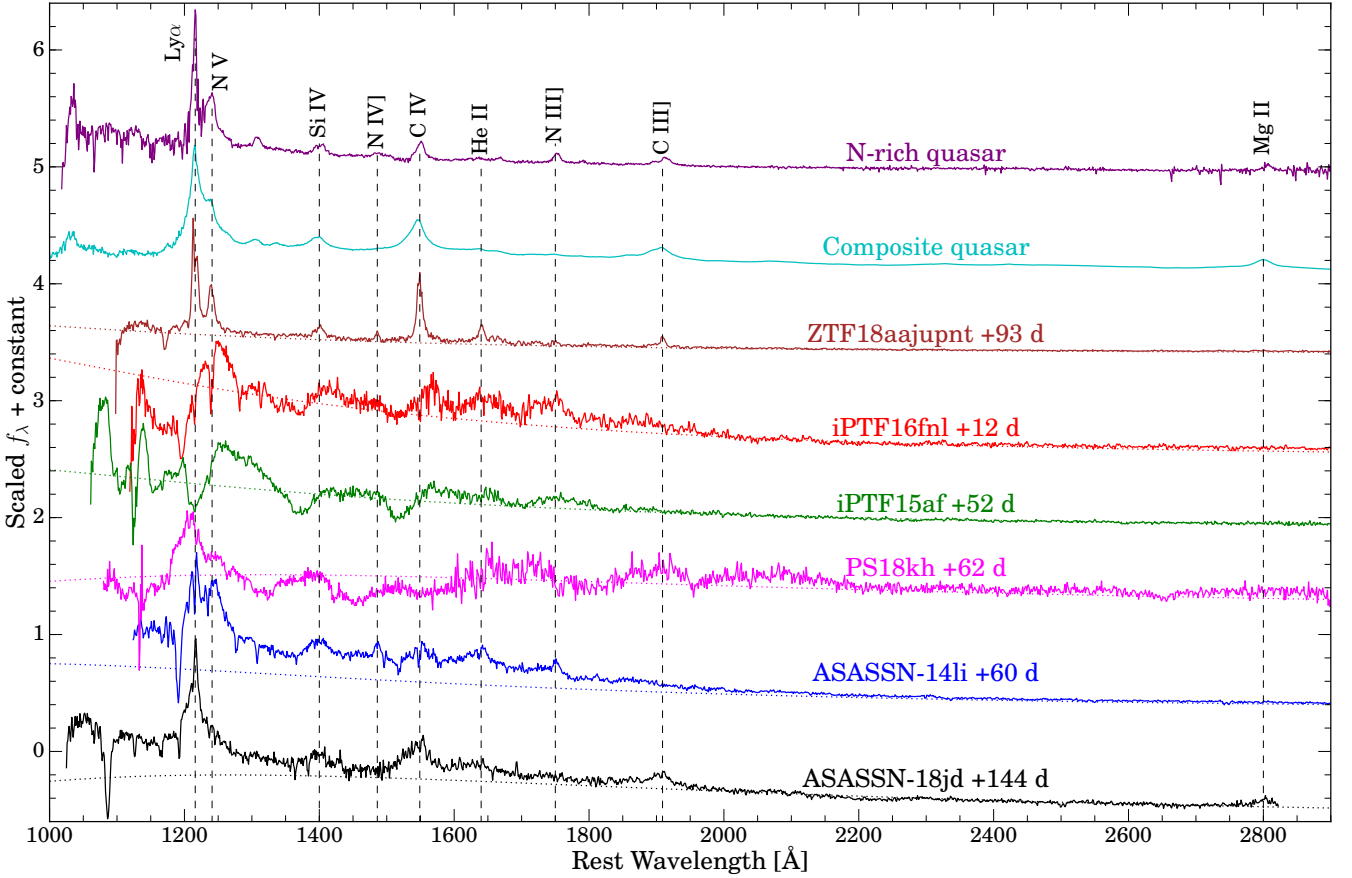


Figure 16. UV spectrum of ASASSN-18jd compared to the UV spectra of known TDEs, the changing-look LINER ZTF18aajupnt, a composite quasar spectrum, and a “N-rich” quasar spectrum. The *Swift*-derived blackbody continuum fits for ASASSN-18jd, the TDEs, and ZTF18aajupnt are shown as dotted, colored lines. Prominent spectral features are labelled.

limit set by the non-detection of X-ray flux was an order of magnitude below the pre-flare detections of the host NLSy1 by *XMM-Newton* from years earlier. The light curve of PS16dtm is similar to that of ASASSN-18jd, in that it faded slowly and also exhibited some bumps inconsistent with monotonic decay. ASASSN-18jd does not, however, show the strong Fe II emission that dominates the spectra of PS16dtm.

As seen in Figure 16, the UV spectrum of ASASSN-18jd is unique compared to that of TDEs. Whereas TDEs do not show lower ionization level lines like O I or Mg II (Cenko et al. 2016; Brown et al. 2018; Blagorodnova et al. 2019), these lines are very common in AGN spectra. Our UV spectra show weak N V $\lambda 1240$ and N III] $\lambda 1750$, and no N IV] $\lambda 1486$ emission. TDEs observed in the UV like ASASSN-14li (Cenko et al. 2016) and iPTF16fnl (Brown et al. 2018) showed strong, broad emission from all of these N lines, especially N V $\lambda 1240$. These emission lines are not seen in iPTF15af (Blagorodnova et al. 2019), which instead showed strong absorption bands like those seen in broad absorption line quasars. UV spectra of PS18kh appear to show strong, somewhat variable N V $\lambda 1240$ emission, but no N III] $\lambda 1750$ or N IV] $\lambda 1486$ emission (Hung et al. 2019). Additionally, our UV spectra show strong C IV $\lambda 1550$ and C III] $\lambda 1909$, the latter of which was not detected in the

other four TDEs. Both of these C III-IV emission lines are common in AGN spectra, while strong N III-IV lines are only seen in the rare N-rich AGNs (e.g., [Batra & Baldwin 2014](#)).

The X-ray light curve of ASASSN-18jd is also unique compared to other X-ray bright TDEs. ASASSN-14li (Holoien et al. 2016a; Brown et al. 2017), *Swift* J1644+77 (Burrows et al. 2005; Bloom et al. 2011; Levan et al. 2016), and *Swift* J2058+05 (Cenko et al. 2012) all exhibited X-ray light curves which decay monotonically and coherently following approximately the canonical $t^{-5/3}$ at early times, irrespective of any short timescale variability (Auchettl et al. 2017, 2018). As ASASSN-14li evolved, its light curve was more consistent with disc emission ($t^{-5/12}$) rather than fall back, but the overall the decay was still monotonic (Auchettl et al. 2017). While the UV/optical emission of ASASSN-15oi showed a steady decay, its X-ray emission did not (Holoien et al. 2016b; Gezari et al. 2017a; Holoien et al. 2018). Its X-ray flux increased around ~ 200 d before decaying ~ 350 d after discovery, which is believed to have been caused by either inefficient circularization that resulted in delayed accretion, or material surround the TDE becoming optically thin a few months after discovery (Gezari et al. 2017b; Holoien et al. 2018). The optically-detected TDEs PS18kh (Holoien et al. 2019a; van Velzen et al. 2019a) and ASASSN-19bt (Holoien et al. 2019b) have also shown X-ray emission, but

only the TDE candidate ASASSN-18ul (Wevers et al. 2019b) exhibits a X-ray light curve similar to that of ASASSN-18jd. ASASSN-18ul shows a relatively flat X-ray light curve with small timescale variations where the X-ray luminosity varies by more than an order of magnitude ($\sim 10^{42} - 10^{43.2}$ erg s $^{-1}$). However, the X-ray spectrum of ASASSN-18ul is different from that of ASASSN-18jd in that it shows no obvious power-law component and has negligible hard X-ray flux.

7.2 ASASSN-18jd as an AGN

As seen in Figures 15 and 16, the spectra of ASASSN-18jd show emission-line features common to AGN spectra, like C III] $\lambda 1909$, and perhaps O I $\lambda 1302$, Mg II $\lambda 2800$, [Fe XIV] $\lambda 5303$, and [Fe X] $\lambda 6375$. Additionally, the narrow [O III] and [N II] emission line strengths are such that they may imply some low level of pre-existing AGN activity. However, the transient nature of the coronal Fe lines and the relatively high ratio of [Fe X] $\lambda 6375$ to [O III] $\lambda 5007$ compared to that seen in narrow and broad line Seyferts can also be interpreted originating from the transient soft X-rays generated by a TDE (Komossa et al. 2009; Wang et al. 2011, 2012). This is due to the gas in the NLR that produces [O III] $\lambda 5007$ being further away from the center of the AGN than the coronal Fe-producing gas, and thus the coronal lines are more sensitive to rapid flares like TDEs.

The X-ray spectra of AGNs share similar properties with ASASSN-18jd, as AGNs often show a combination of a $kT \sim 100$ eV blackbody and a flat power law with $\Gamma \simeq 2$ (Ricci et al. 2017; Aucht et al. 2018). Additionally, the variable hardness ratio and the soft X-ray flare near +140 d are behaviors that are more commonly seen in AGNs than in TDEs (Aucht et al. 2018). However, whereas the softer-when-brighter phenomena in AGNs is attributed to a changing power-law index, ASASSN-18jd shows no such variability in the power-law index, and instead has a fluctuating blackbody component.

While AGNs can vary dramatically, the frequency of the large fluctuations occurring over timescales of under a year is very small. In a survey of SDSS quasars, MacLeod et al. (2012) found that a change in the g band (or in a filter of similar wavelength) of $|\Delta m_g| > 1$ mag in a period of less than 150 d has an occurrence rate of $P \sim 8 \times 10^{-6}$. ASASSN-18jd peaks in g band with roughly $\Delta m_g \simeq 1$ mag, but because of host contamination, the true Δm_g is likely larger. Furthermore, a change in NUV magnitudes of $|\Delta m| > 3.5$ mag, the approximate difference between the measured brightest *Swift* UVM2 and the archival GALEX NUV magnitude, even on the timescale of 1–5 years, has an occurrence rate of $P < 2 \times 10^{-6}$, the sensitivity limit of the survey in MacLeod et al. (2012). In our case, the difference between our *Swift* and archival GALEX photometry is ~ 8 years, but it is likely safe to assume that the NUV flux increased on roughly the same timescale as the optical flux. This makes it unlikely that ASASSN-18jd can be attributed to “normal” AGN variability.

Lawrence et al. (2016) found a sample of “hypervariable” AGNs with $|\Delta m_g| > 1.5$ mag on timescales of 5–10 years, and they attribute some of these flares to changes in accretion state and some to microlensing. Graham et al. (2017) found a similar population of hypervariable AGNs on shorter timescales of 1–3 years, which they attribute to microlensing

and stellar activity, like SNe, stellar-mass BH mergers, and even “slow TDEs”, occurring within the AGNs, rather than intrinsic variability of the AGNs. There are the dramatic changing-look AGNs (e.g., Shappee et al. 2014; MacLeod et al. 2016) which can have large photometric variations on timescales as short as months (Trakhtenbrot et al. 2019b) accompanied by the appearance of a strong UV/optical continuum and broad emission lines. Rapid turn-on events and changing-look LINERs (e.g., Gezari et al. 2017a; Yan et al. 2019; Frederick et al. 2019) show similarly large photometric changes, a transient blue continuum, and broad emission lines, though their host galaxies show no evidence for AGN activity prior to this change. However, changing-look events have spectral lines typical of “normal” AGNs and lack the strong He II and N III seen in the spectra of ASASSN-18jd (e.g., NGC 5548, Dietrich et al. 1993), implying that ASASSN-18jd is distinct from a changing-look event.

7.3 ASASSN-18jd as a new type of transient

Recently, there have been discoveries of UV-bright transients at the centers of galaxies that are either quiescent or contain faint, previously undetected AGNs. These transients are not consistent with known AGN variability or with conventional optically-detected TDEs due to their slow fading timescales and lack of very broad (FWHM $\sim 10^4$ km s $^{-1}$) emission features. Similar to changing-look AGNs/LINERs, these transients are thought to be brought on by a rapid change in the accretion state of the central SMBH.

Kankare et al. (2017) reported the energetic transient PS1-10adi, which rapidly brightened by ~ 2 mag before decaying slowly, smoothly, and exponentially. Its spectra showed features similar to conventional AGNs, with relatively narrow Balmer features and strong Fe II features blueward and redward of H β . While PS1-10adi had a strong blue continuum indicative of a blackbody, the maximum effective temperature was $\sim 1.1 \times 10^4$ K, much cooler than ASASSN-18jd, though not dramatically cooler than the effective temperatures of ASASSN-14ae (Brown et al. 2016) and ASASSN-19bt (Holoien et al. 2019b). Additionally, the light curve of PS1-10adi showed a smooth decay, whereas ASASSN-18jd shows short-timescale fluctuations on top of an overall decay.

Frederick et al. (2019) assigned the transient ZTF18aaajupnt to the newly-defined class of changing-look LINERs, though ZTF18aaajupnt was different from other changing-look LINERs in terms of its evolution and spectral features. ZTF18aaajupnt changed from a LINER to a NLSy1 in < 100 d and showed a blue continuum consistent with a blackbody with $T \sim 4.5 \times 10^4$ K. Its spectra, included in Figures 15 and 16, showed strong, transient He II and coronal Fe lines with relative strengths similar to those seen in ECLEs, as well as strong Mg II $\lambda 2800$ which appeared in the late-time spectra (not shown). ZTF18aaajupnt also showed an increase in soft X-ray flux that began occurring ~ 60 d after the initial UV/optical rise. Compared to most TDEs, it faded relatively slowly (though not as slowly as ASASSN-18jd) and was less luminous. According to the most recent *Swift* observations of this transient, the UV flux has continued to decline whereas the soft X-ray flux has plateaued (Ruan et al. 2019). ZTF18aaajupnt and ASASSN-18jd occurred around SMBHs of similar mass

($10^{7.6} M_{\odot}$), shared transient He II and coronal Fe emission, and had fairly similar UV spectra, but ZTF18aa Jupnt showed no N III emission in its optical spectra or blackbody component in its X-ray spectrum and had much narrower emission lines than ASASSN-18jd.

Trakhtenbrot et al. (2019a) characterized a “new class” of SMBH-driven transients based on the discoveries of three similar events. These events, F01004-2237 (Tadhunter et al. 2017), OGLE17aaJ (Gromadzki et al. 2019), and ASASSN-17cv/AT 2017bgt, were especially interesting because of the presence of strong He II $\lambda 4686$, N III $\lambda 4640$, and N III $\lambda 4100$ emission. OGLE17aaJ and ASASSN-17cv had relatively quick rises to peak brightness over a few months and had UV/optical SEDs that were well fit by $T \sim 10^4$ K blackbodies. They differed from “normal” TDEs because they faded much more slowly, and the broadest components of their optical emission lines resembled those of NLSy1s, with FWHM $\sim 2200 \text{ km s}^{-1}$. ASASSN-18jd shares with these events relatively strong He II and N III emission and a slow fading timescale, but the Balmer features associated with ASASSN-18jd are broader than the Balmer features associated with any of these events and NLSy1s in general.

7.4 Summary

We report the discovery and follow-up observations of the luminous nuclear transient ASASSN-18jd. The most important observed properties of ASASSN-18jd are:

- Archival photometry shows little evidence of strong AGN activity prior to the transient.
- *Swift* UVOT photometry show the continuum emission to be well-modeled by a luminous, $T \sim 2.5 \times 10^4$ K blackbody that fades slowly, with some short-timescale variability. While, the photometry is also well fit by a power-law consistent with an accretion disc, the UV spectra from *HST* show the SED to be more consistent with a blackbody.
- *Swift* XRT and *XMM-Newton* data show widely varying, yet overall fading X-ray emission with $kT \sim 100$ eV blackbody and $\Gamma \sim 1.7$ power-law components. This emission fades by nearly an order of magnitude on a timescale of around 1 year.
- Optical spectroscopy show strong, roughly constant Balmer emission, as well as transient He II $\lambda 4686$, N III $\lambda 4100$, and [Fe X] $\lambda 6375$.

On balance, ASASSN-18jd can be understood as either a TDE or as a new type of SMBH-driven transient. As a TDE, ASASSN-18jd would be one of the most luminous and slowest events known and would challenge the paradigm of TDEs declining rapidly and smoothly. As a new type of transient, ASASSN-18jd would be similar to events like the changing-look LINER ZTF18aa Jupnt and those described in Trakhtenbrot et al. (2019a), yet distinct enough to suggest different conditions driving the event. As ASASSN-18jd continues to evolve, future observations will help us understand the nature of this peculiar transient.

ACKNOWLEDGEMENTS

We thank the *Swift* PI, the Observation Duty Scientists, and the science planners for promptly approving and executing

our *Swift* observations. We thank the *XMM-Newton* team for promptly scheduling and executing our TOO observations. We thank the Las Cumbres Observatory and its staff for its continuing support of the ASAS-SN project.

ASAS-SN is supported by the Gordon and Betty Moore Foundation through grant GBMF5490 to the Ohio State University and NSF grant AST-1515927. Development of ASAS-SN has been supported by NSF grant AST-0908816, the Mt. Cuba Astronomical Foundation, the Center for Cosmology and AstroParticle Physics at the Ohio State University, the Chinese Academy of Sciences South America Center for Astronomy (CASSACA), the Villum Foundation, and George Skestos.

CSK and KZS are supported by NSF grants AST-1515876, AST-1515927, and AST-1814440. CSK is also supported by a fellowship from the Radcliffe Institute for Advanced Studies at Harvard University. KAA is supported by the Danish National Research Foundation (DNRF132). BJS is supported by NSF grant AST-1908952. SD, SB, and PC acknowledge NSFC 11573003. We acknowledge Telescope Access Program (TAP) funded by the NAOC, CAS, and the Special Fund for Astronomy from the Ministry of Finance. MAT acknowledges support from the DOE CSGF through grant DE-SC0019323. CR acknowledges support from the CONICYT+PAI Convocatoria Nacional subvencion a instalacion en la academia convocatoria año 2017 PAI77170080 and from the Fondecyt Iniciacion grant 11190831. PJV is supported by the National Science Foundation Graduate Research Fellowship Program Under Grant No. DGE-1343012. Support for JLP is provided in part by FONDECYT through the grant 1191038 and by the Ministry of Economy, Development, and Tourism’s Millennium Science Initiative through grant IC120009, awarded to The Millennium Institute of Astrophysics, MAS. MRS is supported by the National Science Foundation Graduate Research Fellowship Program Under Grant No. 1842400. MG is supported by the Polish NCN MAESTRO grant 2014/14/A/ST9/00121. The UCSC team is supported in part by NSF grant AST-1518052, the Gordon & Betty Moore Foundation, the Heising-Simons Foundation, and by a fellowship from the David and Lucile Packard Foundation to RJF.

Based on observations made with the NASA/ESA Hubble Space Telescope, obtained at the Space Telescope Science Institute, which is operated by the Association of Universities for Research in Astronomy, Inc., under NASA contract NAS5-26555. These observations are associated with programs GO-14781 and GO-15312.

Based on data acquired using the Large Binocular Telescope (LBT). The LBT is an international collaboration among institutions in the United States, Italy and Germany. LBT Corporation partners are: The University of Arizona on behalf of the Arizona university system; Istituto Nazionale di Astrofisica, Italy; LBT Beteiligungsgesellschaft, Germany, representing the Max-Planck Society, the Astrophysical Institute Potsdam, and Heidelberg University; The Ohio State University, and The Research Corporation, on behalf of The University of Notre Dame, University of Minnesota and University of Virginia. This paper uses data obtained with the MODS spectrographs built with funding from NSF grant AST-9987045 and the NSF Telescope System Instrumentation Program (TSIP) with additional funds from the Ohio

Board of Regents and the Ohio State University Office of Research.

DAHB acknowledges research support through the National Research Foundation (NRF) of South Africa. Some of the observations reported in this paper were obtained with the Southern African Large Telescope (SALT) under the Large Science Programme on transients (2018-2-LSP-001). Polish participation in SALT is funded by grant no. MNiSW DIR/WK/2016/07.

This research has made use of the XRT Data Analysis Software (XRTDAS) developed under the responsibility of the ASI Science Data Center (ASDC), Italy. At Penn State the NASA *Swift* program is supported through contract NAS5-00136.

Observations made with the NASA Galaxy Evolution Explorer (GALEX) were used in the analyses presented in this manuscript. Some of the data presented in this paper were obtained from the Mikulski Archive for Space Telescopes (MAST). STScI is operated by the Association of Universities for Research in Astronomy, Inc., under NASA contract NAS5-26555. Support for MAST for non-HST data is provided by the NASA Office of Space Science via grant NNX13AC07G and by other grants and contracts.

This publication makes use of data products from the Wide-field Infrared Survey Explorer, which is a joint project of the University of California, Los Angeles, and the Jet Propulsion Laboratory/California Institute of Technology, funded by NASA.

This publication makes use of data obtained from the Weizmann Interactive Supernova Data Repository (WISREP, Yaron & Gal-Yam 2012).

REFERENCES

- Andrillat Y., 1968, *AJ*, **73**, 862
- Arcavi I., et al., 2014, *ApJ*, **793**, 38
- Arnaud K. A., 1996, in Jacoby G. H., Barnes J., eds, *Astronomical Society of the Pacific Conference Series Vol. 101, Astronomical Data Analysis Software and Systems V*. p. 17
- Assef R. J., et al., 2013, *ApJ*, **772**, 26
- Auchettl K., Guillochon J., Ramirez-Ruiz E., 2017, *ApJ*, **838**, 149
- Auchettl K., Ramirez-Ruiz E., Guillochon J., 2018, *ApJ*, **852**, 37
- Barron J. T., Stumm C., Hogg D. W., Lang D., Roweis S., 2008, *AJ*, **135**, 414
- Batra N. D., Baldwin J. A., 2014, *MNRAS*, **439**, 771
- Bentz M. C., Peterson B. M., Netzer H., Pogge R. W., Vestergaard M., 2009, *ApJ*, **697**, 160
- Bersier D., Stanek K. Z., 2018, *Transient Name Server Discovery Report*, **2018-555**, 1
- Bianchi S., Guainazzi M., Matt G., Chiaberge M., Iwasawa K., Fiore F., Maiolino R., 2005, *A&A*, **442**, 185
- Bianchi L., Herald J., Efremova B., Girardi L., Zabot A., Marigo P., Conti A., Shiao B., 2011, *Ap&SS*, **335**, 161
- Blagorodnova N., et al., 2017, *ApJ*, **844**, 46
- Blagorodnova N., et al., 2019, *ApJ*, **873**, 92
- Blanchard P. K., et al., 2017, *ApJ*, **843**, 106
- Bloom J. S., et al., 2011, *Science*, **333**, 203
- Boller T., Freyberg M. J., Trümper J., Haberl F., Voges W.,andra K., 2016, *A&A*, **588**, A103
- Bowen I. S., 1934, *PASP*, **46**, 146
- Breeveld A. A., et al., 2010, *MNRAS*, **406**, 1687
- Brown T. M., et al., 2013, *PASP*, **125**, 1031
- Brown J. S., Shappee B. J., Holoiën T. W.-S., Stanek K. Z., Kochanek C. S., Prieto J. L., 2016, *MNRAS*, **462**, 3993
- Brown J. S., Holoiën T. W.-S., Auchettl K., Stanek K. Z., Kochanek C. S., Shappee B. J., Prieto J. L., Grupe D., 2017, *MNRAS*, **466**, 4904
- Brown J. S., et al., 2018, *MNRAS*, **473**, 1130
- Bruzual G., Charlot S., 2003, *MNRAS*, **344**, 1000
- Buckley D. A. H., Swart G. P., Meiring J. G., 2006, in *Society of Photo-Optical Instrumentation Engineers (SPIE) Conference Series*. p. 62670Z, doi:10.1117/12.673750
- Buckley D. A. H., et al., 2018, *MNRAS*, **474**, L71
- Burgh E. B., Nordsieck K. H., Kobulnicky H. A., Williams T. B., O'Donoghue D., Smith M. P., Percival J. W., 2003, in Iye M., Moorwood A. F. M., eds, *Proc. SPIE Vol. 4841, Instrument Design and Performance for Optical/Infrared Ground-based Telescopes*. pp 1463–1471, doi:10.1117/12.460312
- Burrows D. N., et al., 2005, *Space Sci. Rev.*, **120**, 165
- Burrows D. N., et al., 2011, *Nature*, **476**, 421
- Cardelli J. A., Clayton G. C., Mathis J. S., 1989, *ApJ*, **345**, 245
- Cenko S. B., et al., 2012, *ApJ*, **753**, 77
- Cenko S. B., et al., 2016, *ApJ*, **818**, L32
- Chambers K. C., et al., 2016, arXiv e-prints, p. arXiv:1612.05560
- Condon J. J., Cotton W. D., Greisen E. W., Yin Q. F., Perley R. A., Taylor G. B., Broderick J. J., 1998, *AJ*, **115**, 1693
- Crowther P. A., 2007, *ARA&A*, **45**, 177
- Dai L., McKinney J. C., Roth N., Ramirez-Ruiz E., Miller M. C., 2018, *ApJ*, **859**, L20
- DePoy D. L., et al., 2003, in Iye M., Moorwood A. F. M., eds, *Proc. SPIE Vol. 4841, Instrument Design and Performance for Optical/Infrared Ground-based Telescopes*. pp 827–838, doi:10.1117/12.459907
- Denney K. D., Peterson B. M., Dietrich M., Vestergaard M., Bentz M. C., 2009, *ApJ*, **692**, 246
- Dietrich M., et al., 1993, *ApJ*, **408**, 416
- Drake A. J., et al., 2009, *ApJ*, **696**, 870
- Evans C. R., Kochanek C. S., 1989, *ApJ*, **346**, L13
- Finkbeiner D. P., et al., 2016, *ApJ*, **822**, 66
- Flewelling H. A., et al., 2016, arXiv e-prints, p. arXiv:1612.05243
- Frederick S., et al., 2019, *ApJ*, **883**, 31
- Gabriel C., et al., 2004, in Ochsnein F., Allen M. G., Egret D., eds, *Astronomical Society of the Pacific Conference Series Vol. 314, Astronomical Data Analysis Software and Systems (ADASS) XIII*. p. 759
- Gaskell C. M., Rojas Lobos P. A., 2014, *MNRAS*, **438**, L36
- Gezari S., et al., 2017a, *ApJ*, **835**, 144
- Gezari S., Cenko S. B., Arcavi I., 2017b, *ApJ*, **851**, L47
- Graham M. J., Djorgovski S. G., Drake A. J., Stern D., Mahabal A. A., Glikman E., Larson S., Christensen E., 2017, *MNRAS*, **470**, 4112
- Gromadzki M., et al., 2019, *A&A*, **622**, L2
- Guillochon J., Ramirez-Ruiz E., 2013, *ApJ*, **767**, 25
- Hill J. E., et al., 2004, in Flanagan K. A., Siegmund O. H. W., eds, *Proc. SPIE Vol. 5165, X-Ray and Gamma-Ray Instrumentation for Astronomy XIII*. pp 217–231, doi:10.1117/12.505728
- Holoiën T. W.-S., et al., 2014, *MNRAS*, **445**, 3263
- Holoiën T. W.-S., et al., 2016a, *MNRAS*, **455**, 2918
- Holoiën T. W.-S., et al., 2016b, *MNRAS*, **463**, 3813
- Holoiën T. W.-S., Brown J. S., Auchettl K., Kochanek C. S., Prieto J. L., Shappee B. J., Van Saders J., 2018, *MNRAS*, **480**, 5689
- Holoiën T. W. S., et al., 2019a, *ApJ*, **880**, 120
- Holoiën T. W. S., et al., 2019b, *ApJ*, **883**, 111
- Hung T., et al., 2016, *ApJ*, **833**, 226
- Hung T., et al., 2017, *ApJ*, **842**, 29
- Hung T., et al., 2019, *ApJ*, **879**, 119
- Kalberla P. M. W., Burton W. B., Hartmann D., Arnal E. M., Bajaja E., Morras R., Pöppel W. G. L., 2005, *A&A*, **440**, 775
- Kankare E., et al., 2017, *Nature Astronomy*, **1**, 865
- Kara E., Dai L., Reynolds C. S., Kallman T., 2018, *MNRAS*, **474**, 3593

Kastner S. O., Bhatia A. K., 1996, *MNRAS*, **279**, 1137

Kauffmann G., et al., 2003, *MNRAS*, **346**, 1055

Kennicutt Robert C. J., 1998, *Annual Review of Astronomy and Astrophysics*, **36**, 189

Kewley L. J., Dopita M. A., Sutherland R. S., Heisler C. A., Trevena J., 2001, *ApJ*, **556**, 121

Kobulnicky H. A., Nordsieck K. H., Burgh E. B., Smith M. P., Percival J. W., Williams T. B., O'Donoghue D., 2003, in Iye M., Moorwood A. F. M., eds, Proc. SPIE Vol. 4841, Instrument Design and Performance for Optical/Infrared Ground-based Telescopes. pp 1634–1644, doi:10.1117/12.460315

Kochanek C. S., 2016, *MNRAS*, **461**, 371

Komossa S., et al., 2009, *ApJ*, **701**, 105

Koratkar A., Blaes O., 1999, *PASP*, **111**, 1

Korista K. T., Goad M. R., 2004, *ApJ*, **606**, 749

Kovačević J., Popović L. Č., Dimitrijević M. S., 2010, *The Astrophysical Journal Supplement Series*, **189**, 15

Kriek M., van Dokkum P. G., Labbé I., Franx M., Illingworth G. D., Marchesini D., Quadri R. F., 2009, *ApJ*, **700**, 221

Lang D., Hogg D. W., Mierle K., Blanton M., Roweis S., 2010, *AJ*, **139**, 1782

Lantz B., et al., 2004, in Mazuray L., Rogers P. J., Wartmann R., eds, Proc. SPIE Vol. 5249, Optical Design and Engineering. pp 146–155, doi:10.1117/12.512493

Lawrence A., et al., 2016, *MNRAS*, **463**, 296

Leloudas G., et al., 2019, *ApJ*, **887**, 218

Levan A. J., et al., 2016, *ApJ*, **819**, 51

Liu X.-W., Danziger J., Murdin P., 1993, *MNRAS*, **262**, 699

Liu Z., et al., 2016, *MNRAS*, **459**, 1602

Lodato G., Rossi E. M., 2011, *MNRAS*, **410**, 359

MacLeod M., Guillochon J., Ramirez-Ruiz E., 2012, *ApJ*, **757**, 134

MacLeod C. L., et al., 2016, *MNRAS*, **457**, 389

Marchesi S., et al., 2016, *ApJ*, **830**, 100

Martin D. C., et al., 2005, *ApJ*, **619**, L1

McBrien O., Clark P., Kankare E., Yaron O., Knezevic N., 2018, Transient Name Server Classification Report, 2018-587, 1

McClintock J. E., Canizares C. R., Tarter C. B., 1975, *ApJ*, **198**, 641

McConnell N. J., Ma C.-P., 2013, *ApJ*, **764**, 184

Netzer H., Elitzur M., Ferland G. J., 1985, *ApJ*, **299**, 752

Nicholl M., et al., 2019, *MNRAS*, **488**, 1878

Oknyanskij V. L., 1978, *Peremennye Zvezdy*, **21**, 71

Peng C. Y., Ho L. C., Impey C. D., Rix H.-W., 2002, *AJ*, **124**, 266

Peterson B. M., 1993, *PASP*, **105**, 247

Peterson B. M., et al., 2004, *ApJ*, **613**, 682

Phinney E. S., 1989, in Morris M., ed., IAU Symposium Vol. 136, The Center of the Galaxy. p. 543

Pogge R. W., et al., 2010, in Ground-based and Airborne Instrumentation for Astronomy III. p. 77350A, doi:10.1117/12.857215

Poole T. S., et al., 2008, *MNRAS*, **383**, 627

Rees M. J., 1988, *Nature*, **333**, 523

Reynolds C. S., 1997, *MNRAS*, **286**, 513

Ricci C., et al., 2017, *ApJS*, **233**, 17

Roming P. W. A., et al., 2005, *Space Sci. Rev.*, **120**, 95

Roth N., Kasen D., 2018, *ApJ*, **855**, 54

Roth N., Kasen D., Guillochon J., Ramirez-Ruiz E., 2016, *ApJ*, **827**, 3

Ruan J. J., Anderson S. F., Dexter J., Agol E., 2014, *ApJ*, **783**, 105

Ruan J. J., Anderson S. F., Eracleous M., Green P. J., Haggard D., MacLeod C. L., Runnoe J. C., Sobolewska M. A., 2019, arXiv e-prints, p. arXiv:1909.04676

Schlafly E. F., Finkbeiner D. P., 2011, *ApJ*, **737**, 103

Selvelli P., Danziger J., Bonifacio P., 2007, *A&A*, **464**, 715

Shakura N. I., Sunyaev R. A., 1973, *A&A*, **24**, 337

Table 3. Photometry of ASASSN-18jd. All magnitudes are in the AB system and have not been corrected for Galactic extinction or host-subtracted, except for ASAS-SN photometry, which has the observed pre-transient flux subtracted out. Non-detections in ASAS-SN are given as 3σ upper limits. Only a portion of the data is shown here. The entire table is published in machine-readable format in the online journal.

MJD	Filter	Magnitude	Telescope/Observatory
56618.219	V	>18.11	ASAS-SN
56801.576	V	>19.05	ASAS-SN
56805.575	V	>18.95	ASAS-SN
...			
58589.407	i	16.30 ± 0.02	Swope
58636.339	i	16.32 ± 0.02	Swope
58660.258	i	16.32 ± 0.02	Swope

Shappee B. J., et al., 2014, *ApJ*, **788**, 48

Skrutskie M. F., et al., 2006, *AJ*, **131**, 1163

Stern D., et al., 2012, *ApJ*, **753**, 30

Strubbe L. E., Murray N., 2015, *MNRAS*, **454**, 2321

Tadhunter C., Spence R., Rose M., Mullaney J., Crowther P., 2017, *Nature Astronomy*, **1**, 0061

Tohline J. E., Osterbrock D. E., 1976, *ApJ*, **210**, L117

Tozzi P., et al., 2006, *A&A*, **451**, 457

Trakhtenbrot B., et al., 2019a, *Nature Astronomy*, **3**, 242

Trakhtenbrot B., et al., 2019b, *ApJ*, **883**, 94

Vanden Berk D. E., et al., 2001, *AJ*, **122**, 549

Voges W., et al., 1999, *A&A*, **349**, 389

Wang T.-G., Zhou H.-Y., Wang L.-F., Lu H.-L., Xu D., 2011, *ApJ*, **740**, 85

Wang T.-G., Zhou H.-Y., Komossa S., Wang H.-Y., Yuan W., Yang C., 2012, *ApJ*, **749**, 115

Wevers T., van Velzen S., Jonker P. G., Stone N. C., Hung T., Onori F., Gezari S., Blagorodnova N., 2017, *MNRAS*, **471**, 1694

Wevers T., et al., 2019a, *MNRAS*, **487**, 4136

Wevers T., et al., 2019b, *MNRAS*, **488**, 4816

Weymann R. J., Vogel S. N., Veilleux S., Epps H. W., 2001, *ApJ*, **561**, 559

Wilhite B. C., Vanden Berk D. E., Kron R. G., Schneider D. P., Pereyra N., Brunner R. J., Richards G. T., Brinkmann J. V., 2005, *ApJ*, **633**, 638

Woodgate B. E., et al., 1998, *PASP*, **110**, 1183

Wright E. L., 2006, *PASP*, **118**, 1711

Wright E. L., et al., 2010, *AJ*, **140**, 1868

Yan L., et al., 2019, *ApJ*, **874**, 44

Yaron O., Gal-Yam A., 2012, *PASP*, **124**, 668

van Velzen S., et al., 2019a, *ApJ*, **872**, 198

van Velzen S., Stone N. C., Metzger B. D., Gezari S., Brown T. M., Fruchter A. S., 2019b, *ApJ*, **878**, 82

This paper has been typeset from a $\text{\TeX}/\text{\LaTeX}$ file prepared by the author.

Table 4. X-ray Observations of ASASSN-18jd. Non-detections by *Swift* XRT are given as 3σ upper limits. Flux is measured from fitting the individual spectra with a power law + blackbody model for *XMM-Newton*, while for *Swift* XRT, flux measurements assume a power-law spectrum with $\Gamma = 1.75$ (see Section 4). Only a portion of the data is shown here. The entire table is published in machine-readable format in the online journal.

MJD	Exposure [s]	0.3–10 keV Flux [10^{-13} erg cm $^{-2}$ s $^{-1}$]	<i>HR</i>	Telescope
58266.819	28000	1.920 ± 0.101	-0.514 ± 0.011	<i>XMM-Newton</i>
58280.591	21000	2.970 ± 0.355	-0.554 ± 0.009	<i>XMM-Newton</i>
58249.807	2163	1.380 ± 0.560	-0.540 ± 0.094	<i>Swift</i> XRT
...				
58646.995	477	< 1.574	-0.048	<i>Swift</i> XRT
58651.436	2245	< 0.614	0.052	<i>Swift</i> XRT
58661.400	1788	< 0.775	0.090	<i>Swift</i> XRT

Table 5. NUV/Optical Spectroscopic Observations of ASASSN-18jd

Date [UT]	MJD	MJD $-t_0$	Telescope	Instruments	Waverange [\AA]	Resolution [\AA]	Slit Width [$''$]	Exposure [s]
2018-05-13	58251.4	+34.0	du Pont 2.5-m	WFCCD	3600–10000	3	1.5	1x600
2018-05-16	58254.1	+36.7	SALT 10-m	RSS	3700–9000	16	1.5	1x1600
2018-05-16	58254.6	+37.2	U of Hawaii 88-in	SNIFS	3200–10000	7	IFU	1x1200, 1x1600
2018-05-18	58256.6	+39.2	UH88	SNIFS				1x2000
2018-06-11	58280.1	+62.7	SALT	RSS				1x1600
2018-06-12	58281.6	+64.2	UH88	SNIFS				1x1200
2018-06-17	58286.0	+68.6	SALT	RSS				1x1600
2018-06-26	58295.0	+77.6	SALT	RSS				1x1600
2018-07-08	58307.5	+90.1	Shane 3-m	Kast	3500–10000	3	2	3x500
2018-07-11	58310.5	+93.1	UH88	SNIFS				1x1800
2018-07-15	58314.5	+97.1	Shane	Kast				3x600
2018-07-18	58318.0	+100.6	SALT	RSS				1x1600
2018-07-23	58322.6	+105.2	UH88	SNIFS				1x1800
2018-08-02	58332.6	+115.2	SALT	RSS				1x1600
2018-08-14	58344.5	+127.1	UH88	SNIFS				1x2000
2018-08-18	58348.8	+131.4	SALT	RSS				1x1600
2018-09-05	58366.3	+148.9	UH88	SNIFS				1x600, 1x1800
2018-09-25	58386.3	+168.9	UH88	SNIFS				1x1800
2018-10-10	58401.3	+183.9	UH88	SNIFS				1x1800
2018-10-22	58413.3	+195.9	UH88	SNIFS				1x1800
2018-10-31	58422.9	+205.5	SALT	RSS				1x1600
2018-11-05	58427.1	+209.7	LBT 8.4-m	MODS	3200–10000	3	1.0	4x1200
2018-11-06	58428.2	+210.8	UH88	SNIFS				1x1800
2018-12-04	58456.2	+238.8	UH88	SNIFS				1x1800
2018-12-31	58483.2	+265.8	UH88	SNIFS				1x1600
2019-01-03	58486.2	+268.8	UH88	SNIFS				1x1800
2019-01-08	58491.2	+273.8	UH88	SNIFS				1x1200
2019-06-04	58638.3	+420.9	du Pont	WFCCD				3x1200
2019-06-27	58661.0	+443.6	SALT	RSS				1x1800
2019-06-28	58662.4	+445.0	LBT	MODS				3x1200

Table 6. *HST*-STIS Spectroscopic Observations of ASASSN-18jd

Date [UT]	MJD	MJD $-t_0$	Exposure (NUV) [s]	Exposure (FUV) [s]
2018-05-18	58256.8	+39.4	4x169	4x169
2018-06-01	58270.2	+52.8	6x309	6x410
2018-06-28	58297.5	+80.1	6x309	6x410
2018-07-31	58330.9	+113.5	5x375, 5x480	5x497, 5x419
2018-08-14	58344.5	+127.1	5x375, 6x392, 1x370	3x571, 5x471, 3x646, 1x485
2018-08-31	58361.2	+144.7	5x375, 6x392, 1x370	3x571, 5x471, 3x646, 1x485